

Modeling glacial flow on and onto Pluto's Sputnik Planitia[☆]

O. M. Umurhan^{a,b,*}, A. D. Howard^c, J. M. Moore^{a,b}, A. M. Earle^d, O. L. White^a, P. M. Schenk^e, R. P. Binzel^d, S.A. Stern^f, R.A. Beyer^{a,b}, F. Nimmo^g, W.B. McKinnon^h, K. Ennico^a, C.B. Olkin^f, H. A. Weaverⁱ, L. A. Young^f

^aNational Aeronautics and Space Administration (NASA), Ames Research Center, Space Science Division, Moffett Field, CA 94035

^bSETI Institute, 189 Bernardo Ave, Suite 100, Mountain View, CA 94043

^cUniversity of Virginia, Department of Environmental Sciences, P.O. Box 400123 Charlottesville, VA 22904-4123

^dMassachusetts Institute of Technology, Department of Earth, Atmospheric and Planetary Sciences, Cambridge, Massachusetts 02139

^eLunar and Planetary Institute, 3600 Bay Area Blvd. Houston, TX 77058

^fSouthwest Research Institute, Boulder, CO 80302

^gEarth and Planetary Science, University of California, Santa Cruz, CA 95064

^hDepartment of Earth and Planetary Sciences, Washington University, St. Louis, MO 63130

ⁱJohns Hopkins University Applied Physics Laboratory, Laurel, MD, 20723

Abstract

Observations of Pluto's surface made by the New Horizons spacecraft indicate present-day N₂ ice glaciation in and around the basin informally known as Sputnik Planitia. Motivated by these observations, we have developed an evolutionary glacial flow model of solid N₂ ice that takes into account its published thermophysical and rheological properties. This model assumes that glacial ice flows laminarily and has a low aspect ratio which permits a vertically integrated mathematical formulation. We assess the conditions for the validity of laminar N₂ ice motion by revisiting the problem of the onset of solid-state buoyant convection of N₂ ice for a variety of bottom thermal boundary conditions. Subject to uncertainties in N₂ ice rheology, N₂ ice layers are estimated to flow laminarily for thicknesses less than 400-1000 meters. The resulting mass-flux formulation for when the N₂ ice flows as a laminar dry glacier is characterized by an Arrhenius-Glen functional form. The flow model developed is used here to qualitatively answer some questions motivated by features we interpret to be a result of glacial flow found on Sputnik Planitia. We find that the wavy transverse dark features found along the northern shoreline of Sputnik Planitia may be a transitory imprint of shallow topography just beneath the ice surface suggesting the possibility that a major shoreward flow event happened relatively recently, within the last few hundred years. Model results also support the interpretation that the prominent darkened features resembling flow lobes observed along the eastern shoreline of the Sputnik Planitia basin may be the result of a basally wet N₂ glacier flowing into the basin from the pitted highlands of eastern Tombaugh Regio.

Keywords: `elsarticle.cls`, L^AT_EX, Elsevier, template
2010 MSC: 00-01, 99-00

1. Introduction

The New Horizons flyby of Pluto has revealed a planetary surface exhibiting evidence of recent geological activity [1, 2]. In a compendium study found in this volume (Howard et al., 2017, this volume) we have examined the evidence for both ancient and recent glacial flow on Pluto based on imaging data taken by the MVIC and LORRI cameras as well as spectroscopic data obtained by the LEISA instrument. ¹ The aim of this work is to develop a physical model framework to use with investigating

various scenarios pertaining to N₂ ice glacial flow into and within Sputnik Planitia (SP, hereafter and note that all place names on Pluto are informal) ². N₂, CH₄ and CO are observed to be present within and around SP [4] as well as in Pluto's atmosphere [5]. Based on the relative overabundance of N₂ compared to CO on SP, we shall assume that it is the primary material undergoing glacial flow – however, this should be subject to further scrutiny.

Figure 1 depicts a prominent example of features suggesting recent N₂ glacial flow from the pitted uplands of eastern Tombaugh Regio (ETR, hereafter) and down onto the plains of SP. Dark streaks reminiscent of medial moraines, emanating from the highlands, connect to the floor of SP by commonly passing through narrow throats

[☆]All place names of the Pluto system are informal.

*Main contact

Email address: `orkan.m.umurhan@nasa.gov` (O. M. Umurhan)

¹These are cameras and instruments onboard New Horizons: MVIC (Multispectral Visible Imaging Camera) is the medium-resolution color wide-angle “push-broom” camera while LORRI (LOng Range Reconnaissance Imager) is the high resolution framing panchromatic camera. LEISA (Linear Etalon Imaging Spectral Array) is the 256 channel imaging spectrometer [1, 3].

²An earlier version of this manuscript referred to this region as “Sputnik Planum”. The designation of this feature from *planum* to *planitia* is a result of recent topographic refinements indicating that this planar region has an elevation below the mean radius of Pluto.

2-5 km wide. The dark streaks terminate on SP with a pattern resembling flow lobes. There are also lone protruding H₂O ice blocks with trailing dark streaks leading towards the higher elevation N₂ icy flats, highly suggestive that these structures may be englacial debris (Howard et al., 2017, this volume).

Interestingly, flow also appears to be moving from the interior of SP out toward both its northern and southern shores (Howard et al. 2017, this volume). Figures 2(a-b) depict examples of indicators of flow toward Sputnik Planitia’s northern shoreline. The lower portion of Figure 2(a) depicts ovoid patterning interpreted to be downwellings associated with solid-state convection of N₂ ice [1, 2, 6]. However the near shoreline manifestation of the dark patterns takes on a markedly different quality, becoming increasingly wavy closer to shore. Figure 2(b) depicts similar features with the additional appearance of transverse surface patterning suggestive of viscous flow around an obstacle. Two ways in which these observations may be interpreted are: (i) the northward moving N₂ ice flow advects darkened, possibly inactive, convective downwelling zones giving rise to the observed near shoreline gentle undulations or (ii) the wavy patterns are an imprint of topography beneath SP’s surface.

In order to test the viability of scenarios pertinent to Pluto’s apparent present-day glacial flow, a physical model needs to be constructed that takes into account, among other things, the known thermophysical and rheological properties of solid N₂ and CO under the very cold physical conditions of Pluto’s surface. Of the latter molecule, very little laboratory data is available under Plutonian surface conditions, but given CO’s similar molecular bonding structure to N₂, we assume that its behavior resembles that of N₂ under these conditions [2]. Most importantly, however, is the fact that the rheology of solid N₂ has not been very well constrained to date (see discussion in section 2.2) and since many of the results we report in this study depend upon the rheology, any future developments and updates regarding solid N₂’s rheology will likely necessitate revising many of the results quoted here. Despite these current uncertainties, we can use this model to answer some broad qualitative questions about the nature of the observed surface flow.

According to experiments and analyses done to date (see Section 2.2 for further details), N₂ ice behaves as a viscous fluid with a viscosity somewhere between H₂O ice in slightly subfreezing terrestrial conditions ($\eta \sim 10^{12}$ Pa·s at stresses of 10^5 Pa [7]), and room temperature pitch or bitumen ($\eta \sim 10^8$ Pa·s). Conditions affecting the flow of N₂ ice include the depth of the flowing N₂ layers, the incoming geothermal flux and the temperature conditions both at the bases and surfaces of such layers. The layer depth and surface temperatures determine whether or not the N₂ ice moves as a “basally wet”, “wet”, or “dry” glacier, and whether or not a glacier of a given thickness

experiences buoyant solid state convection.³ A preliminary physical model should include other various landform modification processes like accretence/decrecence, i.e., continuous growth/retreat by accretion/decretion, [8], and bedrock scouring. Of course, to what degree these various landform modifying effects are operating on today’s Pluto is unclear, but we formally include it in our construction with the expectation that these inputs will become clear once more research is done.

With today’s surface temperature on Pluto being ~ 38.5 K, [4], getting solid N₂ to surpass its triple point at the base of the layer requires layer thickness of up to 0.1-1km or more [2, 6]. N₂ collected on sloping channels will likely advect into depressions (including SP) long before one can build up that much material owing to the apparent low viscosity of solid N₂. However, occasional basal melt of N₂ ice layers in the pitted highlands surrounding SP may have occurred in Pluto’s recent geologic past. Two recent studies, [9] and (Earle et al., 2017, this volume), have shown that Pluto’s obliquity variations [10] coupled with the precession of Pluto’s orbital apsis can give rise to conditions in which Pluto’s surface temperatures might get as high as ~ 55 -60 K for stretches of time lasting 2-3 decades. Under those conditions, N₂ ice layers as little as 200-400 meters thick may undergo basal melt which could give rise to episodic, possibly flood-like, drainage events. Similarly, however, basal melt can also result in steady-state drainage of liquid N₂ into the H₂O ice bedrock below – especially if the substrate is highly porous and/or supports a deeply extended crack system.

At this early stage of discovery, these observations and reflections point to many questions about the history and conditions of N₂ ices on Pluto. In this study we start with two modest scenarios which we examine using a vertically integrated physical model whose development is detailed in section 4. The two questions we seek to address with our mathematical model are

1. Are the transverse wavy dark features near the northern edges of SP an imprint of bottom topography?
2. Are the flow lobe features and deposits indicated by similarly darkened features in Figure 1 evidence of basal melting and consequent basal sliding style flow?

The short answer to each question is: (a) Our model results show that bottom topography can be embossed on the surface of flowing N₂ ice. However, due to the viscous nature of the ice, the imprint fades in a few decades suggesting that such features are transitory and short. (b) A scenario in which N₂ ice flows as a basally wet glacier, i.e., a glacier whose base is in a liquid state, better reproduces the quality of the observed flow lobe features, however, it

³A basally wet glacier here is understood to be a glacier whose base is liquid. This should be distinguished from a wet glacier which is, throughout its entirety, a mixture of ice and liquid between ice grains.

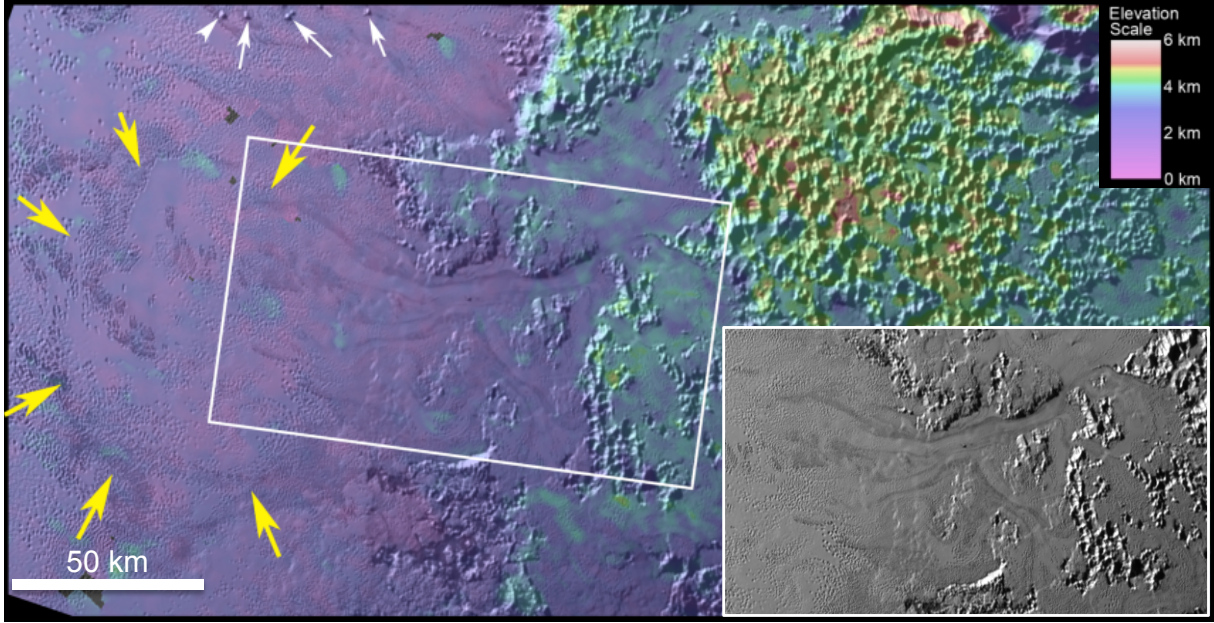


Figure 1: A LORRI image section of eastern Sputnik Planitia abutting the pitted highlands of ETR color-coded for elevation. Streak patterns emanating from the higher elevations are seen to follow an apparent flow path to the lower reaches of Sputnik Planitia. Yellow arrows indicate the extent of flow lobes. Examples indicating englaciated debris shown with white arrows. In this image, north is up. Location of this section is found in Fig. 3.

does not rule out that the observed features are a result of purely dry glacial flow.

This work is organized in the following way. In section 2, we review known relevant information on solid N_2 and CO , and we provide a table summarizing their thermophysical properties. Section 2.2 provides a summary of the current knowledge of N_2 rheology including estimates of its stress-strain rate relationships as well as the corresponding viscosities. Section 2.3 discusses the near surface thermal profiles likely to be present within N_2 ice. Section 2.4 considers the range of possible surface temperatures on Pluto over the course of its obliquity variations over the last 3 million years. Section 3 examines the conditions for the onset of thermal convection in N_2 ice heated from below by a static H_2O ice bedrock conducting Pluto’s geothermal heat-flux. The answer to this question is important because it determines the validity of the glacial model developed in the section that follows.

Section 4 contains a description of the flow model and mass-flux law we construct for N_2 glacial flow appropriate for the surface of Pluto followed by an examination of various e-folding relaxation timescales for N_2 ice structures of various sizes, depths and extents using the formulated mass-flux law. Owing to its highly technical nature, we have relegated to Appendix C the detailed mathematical development of the vertically integrated flow model we adopt which includes the primary assumption that the flow is laminar, neither experiencing buoyant convection nor shear flow induced turbulence. Section 5 begins with detailing the model landscapes we use for our simulations

and is concluded by model results concerning the two hypothetical questions posed above. Section 6 reviews our efforts and rounds out with some thoughts on future directions.

2. General physical properties

2.1. Thermophysical properties of N_2 and CO

N_2 and CO have similar molecular bond physics (primarily Van der Waals) and their collective properties as a solid ought to be similar to one another. However, while some laboratory data is available for N_2 at the temperatures and pressures of relevance for Pluto, comparatively scant laboratory data is available for CO . Nonetheless, we have compiled and summarized this data in tabular form in Table 1. We note an important quality of N_2 , namely that it is relatively insulating compared to H_2O ice: in fact the conductivity of nitrogen ice is $K(N_2) \approx (1/20)K(H_2O)$, where the figure for H_2O ice conductivity $K(H_2O)$ in the temperature range 36-63 K is taken from reference [11]. It is also noteworthy that the coefficient of thermal expansion of nitrogen ice is also nearly 5 times that of H_2O ice at these temperatures.

Both N_2 and CO have two solid phases: α and β . The crystal structure of the α phase is cubic while the β phase is a hexagonal close-packed crystal [12, 13]. The $\alpha - \beta$ phase transition in CO occurs at $T = T_{\alpha\beta}(CO) = 61.55$ K while the corresponding transition occurs for N_2 at $T = T_{\alpha\beta}(N_2) = 35.6$ K [14] with transition enthalpies of 22.4 kJ/kg and 8.2 kJ/kg for CO and N_2 respectively [13, 15].

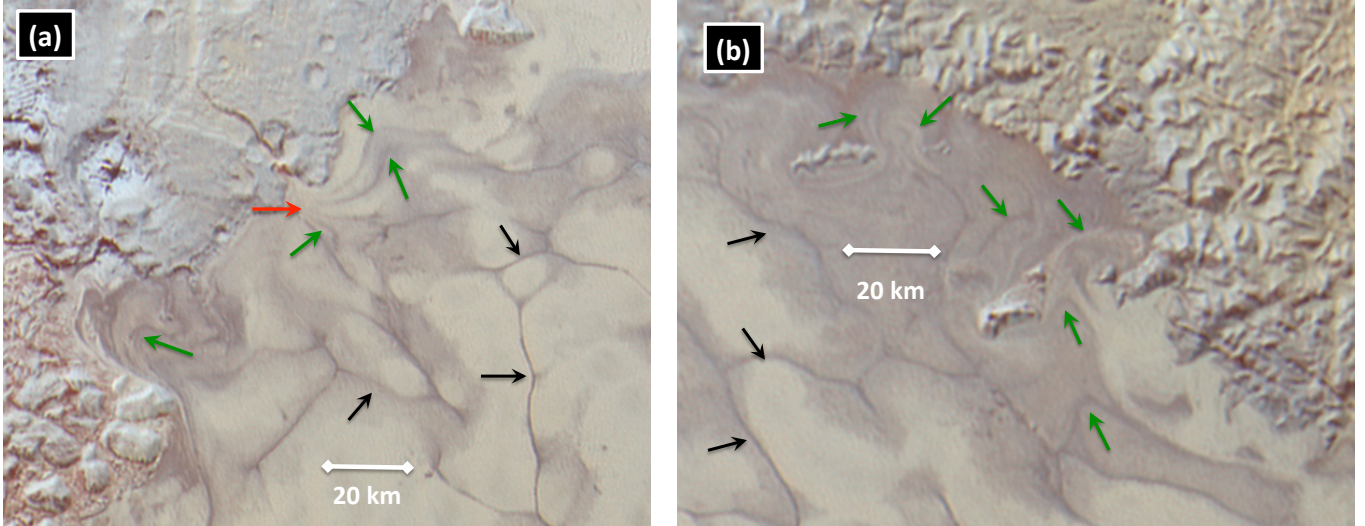


Figure 2: MVIC sections of the northwestern (left panel) and northeastern (right panel) shorelines of Sputnik Planitia. The dark ovoid pattering found on the lower portion of both images (black arrows) have been interpreted as downwellings involving solid-state convection of N_2 ice [6]. The near shoreline dark pattering (green arrows) may be indicative of either flow advection of recently inactivated convective downwellings or an imprint of surface topography beneath the observable surface. The red arrow indicates a possible undersurface drainage point (Howard et al. 2017, this volume). In both images, north is up. Location of this section is found in Fig. 3.

We note that the surface pressures are sufficiently low as to not effect the quality of the emerging crystal structure [12]. It is also worth noting that for the surmised surface temperatures of Pluto, CO is in its α -phase while N_2 is in its β phase. While CO and N_2 are fully soluble in the range of temperatures of interest to us, the rheological properties of a composite mixture of the two molecular species is currently unknown, requiring detailed laboratory work in the near future. The uncertainty in the rheological properties are likely compounded when a third constituent, like CH_4 , is added to the mix.

2.2. Rheological properties of N_2 and CO

As of the writing of this work, there are two known studies pertaining to the rheological properties of N_2 in solid-state for the temperatures of interest to us, i.e. between 30 K and 63 K. There is no known analogous laboratory analysis of CO.⁴ As such, and primarily owing to the similar molecular bond structures of both N_2 and CO (see last section), we cautiously consider the qualitative and quantitative properties of CO ices to be similar to N_2 . We briefly review the aforementioned N_2 studies here:

Non-newtonian creep of laboratory annealed solid N_2 . [20] consider the rheological properties of laboratory annealed N_2 under a variety of tangential stresses and at two temperatures (45 K and 56 K). They show that its stress, σ , and strain-rate, $\dot{\epsilon}$, behave with a power-law relationship given by

$$\dot{\epsilon} = A(T)\sigma^n(T), \quad (1)$$

where the prefactor A and the index n (in the vicinity of 2.1) are both temperature dependent. The prefactor $A(T)$ was fit to an Arrhenius form in [2] and shown to have an effective activation energy E_a of about 3.5 kJ/mole or, equivalently

$$A(T) = A_{45} \exp\left(\frac{T_a}{45 K} - \frac{T_a}{T}\right),$$

$$A_{45} = 0.005 s^{-1} (\text{MPa})^{-n(T)}, \quad (2)$$

where the activation temperature is $T_a = E_a/k = 422 K$. The temperature dependence of the index was determined assuming a linear fit to be given by the expression $n(T) = 2.1 + 0.0155(T/K - 45)$. With this in mind, we assume a *visco-plastic viscosity* which is defined as

$$\eta \equiv \frac{\partial \sigma}{\partial \dot{\epsilon}}, \quad (3)$$

[21]. Together with this we input the power-law form for the laboratory annealed N_2 ice experiment to find

$$\eta = \frac{1}{nA\sigma^{n-1}}. \quad (4)$$

Under conditions where the tangential stresses are about 10 kPa (0.1 bar) the viscosity of N_2 ice at 45 K is about 1.6×10^{10} Pa.s.

Newtonian creep of N_2 ice grains. In [22, 23, 24] the rheological properties of N_2 ice grains were examined in the framework of both Coble creep and Nabarro-Herring (NH) creep, both considered diffusional processes ($n = 1$) and often considered collectively as grain-boundary sliding (GBS) [7]. As opposed to the non-Newtonian case just discussed, we assume the viscosity of grains is linear (and,

⁴Probably owing to its hazardous biological toxicity.

Table 1: Known properties of solid N₂ and CO near their triple points

Molecule	T_m/P_m ^a (K/bars)	ρ_s (g/cm ³)	C_p (kJ/kg·K)	K (W/mK)	α ^b ($\times 10^{-3}/K$)	ΔE_s ^c (kJ/kg)	ΔE_f ^d (kJ/kg)
N ₂	63.10/0.11 ^e	0.99-0.95 ^g	1.35-1.65 ^g	0.215-0.200 ^g	1.7-2.7 ^g	224.9 ^h	25.7 ^h
CO	68.13/0.14 ⁱ	1.01-0.97 ^j	1.29-2.32 ^{k,l}	0.350-0.280 ^m	n/a	296.4 ^l	29.6 ⁿ

^a Melt temperature and pressures at triple point.

^b Coefficient of thermal expansion.

^c Heat of sublimation in vicinity of T_m .

^d Heat of fusion in vicinity of T_m .

^e Ref. [14].

^g Range quoted for β -phase of N₂ between 36-63 K, ref. [12].

^h Ref [15].

ⁱ See [14, 16]

^j Range quoted for α -phase of CO between 41-61.5 K, based on compiled data shown in Fig. 1 of ref. [13].

^k Note that in α -phase these quantities deviate from linear profile.

^l Experimentally determined, ref. [13, 17]

^m Range quoted for α -phase of CO between 45-65 K, based on experimental data shown in Fig. 4 of Ref. [18].

ⁿ Ref. [19].

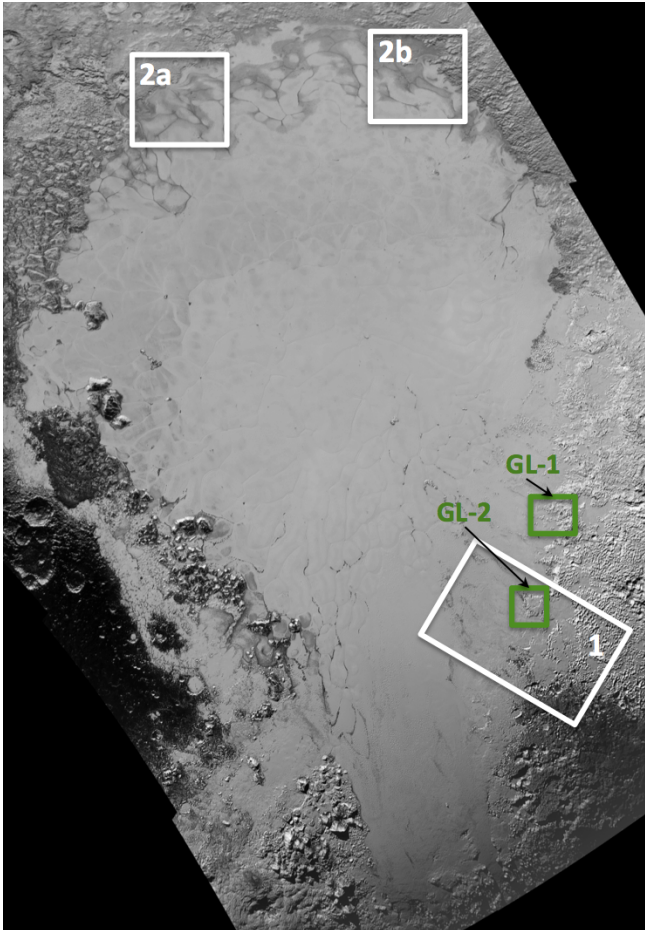


Figure 3: A larger view of Sputnik Planitia with the locations of Figures 1-2 indicated (white boxes). The green boxes indicate sample landscapes (“GL-1”, “GL-2”) are used as test bedrock landforms for modeling done in section 5.

hence, “Newtonian”). The grain rheologies discussed in these aforementioned studies are based on a nuclear magnetic resonance (NMR) study of N₂ grains done by [25]. Coble creep is based on the diffusion of molecules *along* grain boundaries while NH creep is based on the diffusion of molecules *through* grains themselves. The general trend is that NH-creep dominates Coble creep when a material approaches its melt temperatures. Based on the scant data available for N₂, NH creep will dominate Coble creep for temperatures greater than about 25K for grain diameters in the vicinity of 1mm (see Appendix A).

Thus, for N₂ ice grain spheres of radial size d_g the effective volume diffusion rate through grains D_{0v} was empirically assessed by [25] (studying the self-diffusion of N₂ ice laced with Ar impurities) to be given by

$$D_{0v} = 1.6 \times 10^{-7} e^{-T_v/T} \text{ m}^2/\text{s}, \quad (5)$$

where the experimentally determined activation temperature $T_v \approx 1030\text{K}$ relates to the corresponding experimentally determined activation energy, $E_v \approx 8.6\text{kJ/mole}$, via $E_v \equiv kT_v$, where k is the Boltzmann constant ($= 1.38 \times 10^{-23}\text{m}^2\text{kg s}^{-2}\text{K}^{-1}$). From this relationship an effective *linear viscosity* can be written as [23, 24]

$$\eta = \frac{kTd_g^2}{42D_{0v}\Omega}, \quad (6)$$

where Ω is the volume of a single N₂ molecule ($= 4.9 \times 10^{-29}\text{m}^3$). This expression can be rewritten in a way more revealing and relevant to the surface of Pluto

$$\eta_{nh} = 1.84 \times 10^{16} \left(\frac{d_g}{\text{mm}} \right)^2 \left(\frac{T}{45 \text{ K}} \right) \exp \left(\frac{T_v}{T} - \frac{T_v}{45 \text{ K}} \right), \quad (7)$$

in units of Pa · s. We have designated this effective viscosity η_{nh} in order to make it clear that this is the purely “Newtonian”, diffusion creep instance of this form.

While the non-Newtonian properties of N₂ ice grains are not fully explored beyond that described above, we posit, by analogy to extensive studies done on the creep properties of H₂O ice, that diffusion GBS creep of N₂ ice grains may be enhanced by dislocation accommodated GBS. Assuming that the stresses in subsurface Plutonian ices sit well within the range of 1 - 10⁵ Pa and the grain

sizes are within 0.001 to 1 mm, and accepting the posited analogy between N_2 and H_2O ices, an examination of the various expected rheological properties of H_2O ices showcased in Figure 6 of [7] suggests that N_2 ice grains might have a “superplastic” weakly non-Newtonian flavor with a stress-strain power-law index of $n = 1.8$. Provided this is the case for N_2 ice grains, then according to the definition of viscosity in Eq. (3) we suggest that their collective viscous behavior might be described by

$$\eta = \eta_{nh} \left(\frac{\dot{\epsilon}_2^{(nh)}}{\dot{\epsilon}_2} \right)^{(1-n)/n} = \eta_{nh} \left(\frac{\dot{\epsilon}_2^{(nh)}}{\dot{\epsilon}_2} \right)^{-4/9}, \quad (8)$$

where $\dot{\epsilon}_2^{(nh)}$ is a reference value of the second invariant of the strain tensor, a figure currently unknown and requiring future laboratory work to determine.

2.3. On the thermal profiles of Plutonian N_2/CO ice layers

The thermal gradients and timescales of N_2/CO ice-layers are important to assess. Assuming ice-layers too shallow for convection to occur, we can estimate the vertical temperature gradient across a layer of depth H . A recent study by [26], investigating the interior thermal history of Pluto, suggests that the current-day geothermal heat-flux amounts to a few $10^{-3} W/m^2$. We adopt as a reference value for this interior flux of $F_{P1}^{(ref)} = 4 \times 10^{-3} W/m^2$. From the numbers compiled in Section 2.1 for N_2 ⁵, we adopt a value for the conductivity $K \approx 0.2 W/mK$ and assigning F_{P1} to be the emergent heat flux, we find that the mean interior temperature gradient $\bar{T}_z \equiv F_{P1}/K$, or

$$\bar{T}_z \approx 20 \left(F_{P1}/F_{P1}^{(ref)} \right) \text{ } ^\circ K/km. \quad (9)$$

We note that due to its insulating nature compared to H_2O ice, the vertical temperature gradient in such ices is very high. The thermal diffusion coefficient through solid N_2 can be estimated from the definition $\kappa \equiv K/\rho_s C_p \approx 0.66 \times 10^{-6} m^2/s$ where we adopt a value for the heat capacity $C_p = 1.65 kJ/kg K$. Thus, one can estimate the e-folding thermal relaxation time across a layer of width H by $\tau \equiv H^2/(4\pi^2\kappa)$, which we express as [2],

$$\tau = 6 \times 10^{-3} (H/m)^2 \oplus yr = (H/H_0)^2 \oplus yr, \quad (10)$$

in which $\oplus yr$ is one terrestrial year. The reference scale $H_0 \approx 12.9 m$, which says that a layer of approximately 13 meters will equilibrate into its conductive profile in one Earth year. Thus, unless deposition rates greatly exceed this figure, the temperature profile of the glacier should be roughly equal to the conductive equilibrium profile. Calculations performed and quoted by [27] and [4] estimate sublimation/deposition rates on present-day Pluto to be in the range 1-10 cm/yr which suggests that it is reasonable to assume a glacier whose interior temperature is in conductive equilibrium.

⁵Keeping in mind that all quoted quantities have a temperature dependence but we consider them sufficiently weak for our current considerations.

2.4. Surface temperatures over time

We undertake a momentary detour in our discussion and consider the past history of Pluto’s surface temperatures. The import of this consideration is to give a justification for the potential of N_2 ice glaciers to undergo basal melt for certain stretches of time (see Section 4). The idea we have in mind here is the following: with the emerging geothermal flux held fixed, a rise in the surface temperature will steadily induce a concomitant rise in the temperature of the base. Thus, even if the surface does not approach melting point, the base of the glacier will more easily achieve this state owing to its relative warmth. With a wet base, the flow and evolution properties of N_2 glaciers will exhibit significantly different qualities from those glaciers that remain basally frozen.

While the surface temperature of today’s Pluto is just under 40 K, the surface was likely to be much warmer in its past. Pluto’s obliquity variations [10] coupled with the precession of its orbital apsides implies that the total amount of seasonally averaged radiant energy received on a given hemispheric surface will significantly vary over timescales of approximately three million \oplus years. This has direct influence on the resulting surface pressures and temperatures [9] and can give rise to surface temperatures approaching 55-60 K lasting for about 20-30 Pluto years under conditions of favorable alignment of Pluto’s orbital apsis and obliquity extremes.

Figures 4a-b show the surface temperature results of two Pluto climate models whose details may be found in Earle et al. (2017, This Volume). The model, based on the one constructed by [28], and its parameter inputs are summarized here: Pluto’s heliocentric distance and sub-solar latitudes are calculated as a function of time based on the calculation of [29]. A simplified albedo and volatile map is used which assumes polar caps with latitudinal extent of either ± 45 (Fig. 4) or ± 60 (Fig. 4b). The polar caps are modeled as having a variety of different albedos (0.1, 0.3, or 0.6). To represent the thermal influence of Tombaugh Regio, Earle et al. (2017, this volume) include a bright (albedo=0.6) volatile patch extending from -30 degrees to $+45$ degrees with a longitudinal extent of 45 . For different trials, two extremes of a range of plausible emissivity values are examined (e.g. 0.6 or 0.9). These inputs are then incorporated into the energy balance equation model, originally presented in [28], and used to determine the global temperature as a function of time. Note that the solutions developed do not take into account the possibility of time lags associated with thermal inertia effects.

The results are fairly typical: During extreme insolation conditions when Pluto’s orbital apsides and obliquity are favorably aligned, maximum surface temperatures persist for 20-30 Pluto years. When the polar caps extend to ± 60 latitude, the surface temperatures become very close to the melt temperature of N_2 . This means that one may have circumstances in which *relatively shallow* layers of N_2 ice may experience basal melting for stretches of time and

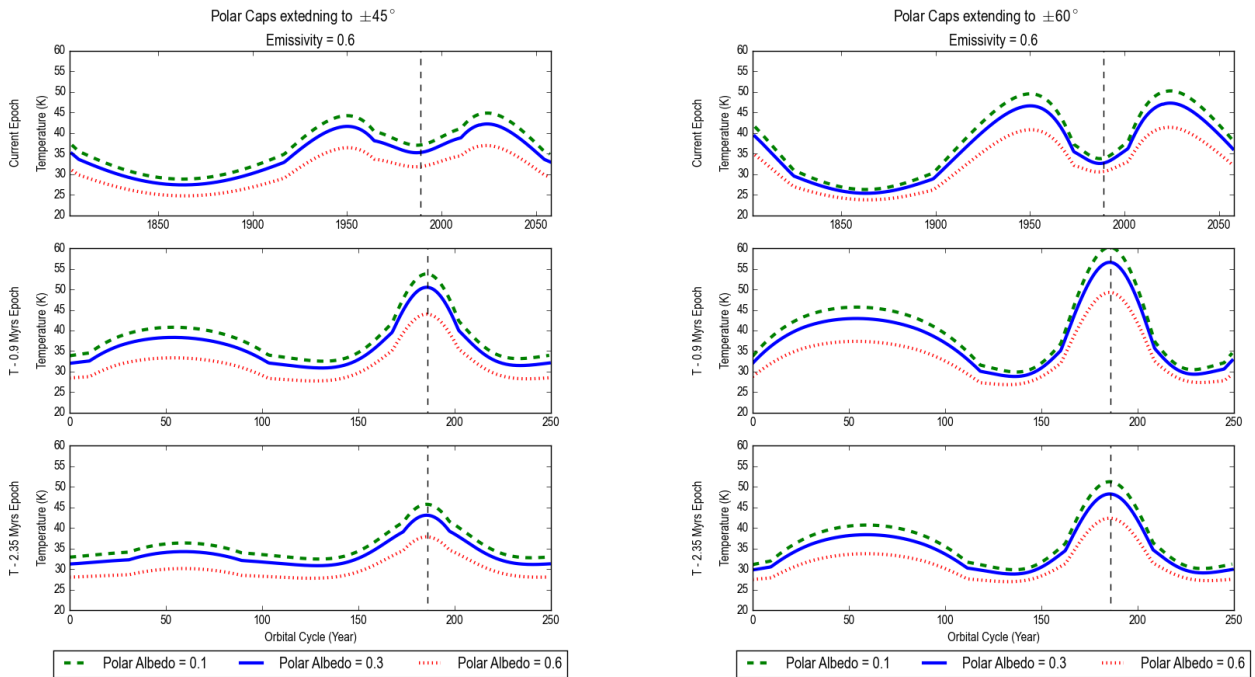


Figure 4: Surface temperatures of Pluto over a 3 Myr obliquity/precessional cycle. Model assumes the presence of a landmass representing Tombaugh Regio (see text). The ice emissivity is assumed to be 0.6. Solutions are shown for three different values of the polar albedos. Left panel shows a suite of solutions assuming that the polar caps extend down to $\pm 45^\circ$ latitude while right panel shows solutions with the polar caps extended further to $\pm 60^\circ$ latitude.

this, in turn, can have important physical consequences in the flow response of N_2 ice layers, i.e., whether or not the layer exhibits basally wet or dry flow – see further discussion of this in section Appendix C.1.

For example, during these climate extremes, the surface temperatures get as high as 55K which, assuming a conductive temperature gradient within the ice of 20 K/km, would correspond to a layer thickness just under 400 m before melt occurs at the base of the glacier (the minimum pressure requirement for melt, of about 10^4 Pa [14], is satisfied at that depth).

3. Onset of convection

The eastern shoreline of SP, and various locations along the other boundaries of SP, indicate there are regions in which convection is either absent or occurring very weakly [6]. While the subsurface basin profile of SP is unknown, estimates as to the depth of various sections of SP can be made based on the distinctive lack of obvious signs of buoyant solid-state convection. One of the important inputs for this study is to estimate an upper limit of the thickness of an N_2/CO ice layer before it starts to undergo solid-state convection. In addition to knowing when one ought to expect convection to occur in, SP the glacial flow modeling detailed in Section 4 also implicitly assumes that the flowing glacial ice is more or less laminar, which we assume to be the case if the layer thicknesses are less than that for

onset of convection. It is therefore important to get a good sense of the conditions under which convection is expected to occur. Thermal convection in terrestrial ice glaciers has been examined as a possible explanation for the origin of ice streams which can drain up to 90% of glacial ice [21].

It is not useful to perform here an exhaustive examination of the transition into convection given all the possible formulations of N_2 's rheology outlined in Section 2.2. We are interested, however, in getting a good order of magnitude figure for this onset. Thus for our calculation here we assume a static Newtonian layer of N_2 ice grains and consider the onset to convection assuming the viscosity is given by $\eta = \eta_{nh}$, as defined in Equation (7). This analysis then becomes amenable to a linear stability calculation. We assume the layer is in conductive thermal equilibrium with its interior which is a reasonable assumption given the thermal equilibration times we estimated in the previous section. The vertical horizontally uniform temperature profile is $T(z) = T_s - \bar{T}_{oz}(z - z_s)$ where \bar{T}_{oz} is given in Eq. (9), z_s is the location of the surface, and T_s is the temperature of the surface for which we set as the present day surface temperature on N_2 ice of 38.5 K.

Due to the temperature contrast, the viscosity at the top and bottom of a layer will be different and, therefore, we consider the Rayleigh number Ra as measured at the base of a given layer. We hereafter consider the viscous diffusion $\nu \equiv \eta/\rho_s$ and define $p \equiv \ln(\nu_t/\nu_b)$ to be the natural logarithm of the ratio of the viscosities between

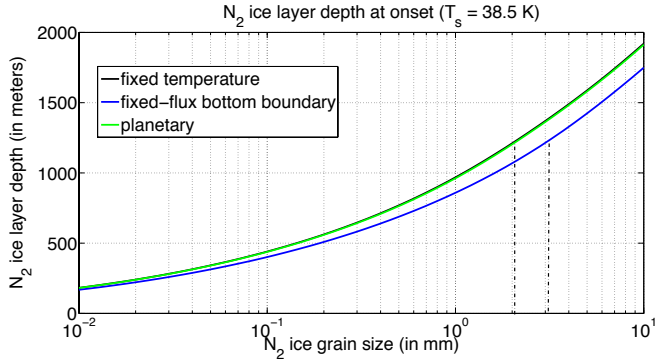


Figure 5: Minimum layer thickness for the onset of convection as a function of N_2 ice-grain size. Figure shows solution of transition to convection assuming the top of the convecting layer has fixed upper temperature of $T = 38.5\text{K}$ and vertical temperature gradient $\bar{T}_{0z} = 20\text{K/km}$. Solutions for three different bottom thermal boundary conditions shown: fixed-temperature, fixed-flux and “planetary” – detailed in Appendix B. Solutions determined use the Frank-Kamenskii approximation [30]. Vertical hatched lines denote critical grain-sizes for which the temperature at the layer’s base corresponds to $T_m = 63.1\text{K}$, i.e., the triple-point melt temperature for N_2 .

the top and bottom layers, ν_t and ν_b respectively. The Rayleigh number Ra at the base is therefore defined as

$$Ra \equiv \frac{g\alpha H^4 \bar{T}_{0z}}{\kappa \nu_b}, \quad (11)$$

where $g = 0.642\text{m/s}^2$ is the surface gravity of Pluto and α is the coefficient of thermal expansion whose values of N_2 ice are given in Table 1. The onset to convection is a function of the two parameters p and Ra . We note that Ra has an Arrhenius law dependence due to the temperature dependence on ν_b , as well as a d_g^{-2} dependence on ice-grain size. The detailed form of Ra , as well as the assumptions and solution methods employed to assess this transition to convection, is detailed in Appendix B.

We are interested here in three questions: (1) For a given N_2 ice-grain size d_g , how deep a layer of N_2 ice on Pluto does one need to initiate solid-state convection? (2) At onset of solid-state convection, what is the critical viscosity contrast as a function of d_g ? (3) What is the temperature of the base of the layer at onset to convection as a function of d_g ? The answer to these questions are graphically displayed in Figures 5-6 and we use these figures for our future referencing henceforth. We note that the depth of the ice-layer must be thicker for larger ice-grains and this is to be expected since solid-state ices composed of larger ice-grains are characterized by larger viscosities.

We also note there are critical values of the ice-grain size for which the transition into convection occurs at depths for which the base temperature, $T_b \equiv T_s + H\bar{T}_{0z}$, corresponds to the melt temperature T_m at the triple-point for N_2 . The bottom panel of Figure 6 shows the results of a model in which the surface temperature $T_s = 38.5\text{K}$ and where $\bar{T}_{0z} = 20\text{K/km}$, and we see that T_m corresponds to about 63 K for ice-grains of size $d_g = 2 - 3\text{mm}$ (depend-

ing upon which boundary condition is employed). Cross-referencing this critical grain-size with the corresponding critical value of the depth of the layer upon which transition is predicted to occur (Fig. 5) shows that this happens at layer thicknesses $H \approx 1.2\text{km}$.

We conclude by noting that the onset of convection in sheared flows is known to occur at (and often significantly) higher values of Ra as compared to their non-sheared equivalents, e.g., see the discussion and references in [31, 32]. As such, we consider the Ra numbers for transition to be lower bounds for the onset of convection in down-gradient flowing N_2/CO ice. In practice this means for us that flowing ice layers probably move laminarily down-gradient for layer thicknesses greater than the limits suggested by conditions indicated in Fig. 5. When revisions to N_2 rheologies become available, many of the figures quoted in this work will need to be revised.

4. Landform evolution modeling

Partly motivated by our findings regarding the onset of convection described in Section 3, we treat the glacially flowing ice as a single laminarily flowing viscous fluid in the infinite Prandtl number limit. This assumption permits the use of vertically integrated modeling methods (e.g., see discussions in [33, 34]) whose asymptotic validity is rooted in perturbation analyses (e.g., [35]). The assumption of laminar flow is valid so long as the moving glacial ice layers are not thick enough to experience buoyant convection. Vertically integrated modeling is expected to be valid so long as the horizontal length scale of the layer dwarves the vertical extent of the layer – in the glaciology literature this is often referred to as the shallow sheet approximation (SSA) [33]. Appendix C contains a detailed exposition of the derivation of the vertically integrated SSA model we use and interested readers are directed there.

The model setup is sketched in the cartoon found in Fig. 7. We consider a single spatiotemporally varying ice component whose local vertical thickness as a function of horizontal location is given by $H(x, y, t)$. The ice sits on a bedrock whose surface is located at $z = Z_b(x, y, t)$. Note in Appendix C we develop a model in which the bedrock may be convertible into ice due to various landform modifying processes, but for our purposes here in this study we treat the bedrock as static. The local elevation is given by $z = Z(x, y, t) = H(x, y, t) + Z_b(x, y)$. The evolution of the local ice layer is given by the (scaled) horizontal divergence of the corresponding mass flux

$$\partial_t H = \nabla \cdot \mathbf{q}, \quad (12)$$

where the *total mass-flux* is given as the sum of a “dry” and “basally wet” glacial flow,

$$\mathbf{q} = q_0 \nabla Z, \quad q_0 = q_{sl} + q_{dry}. \quad (13)$$

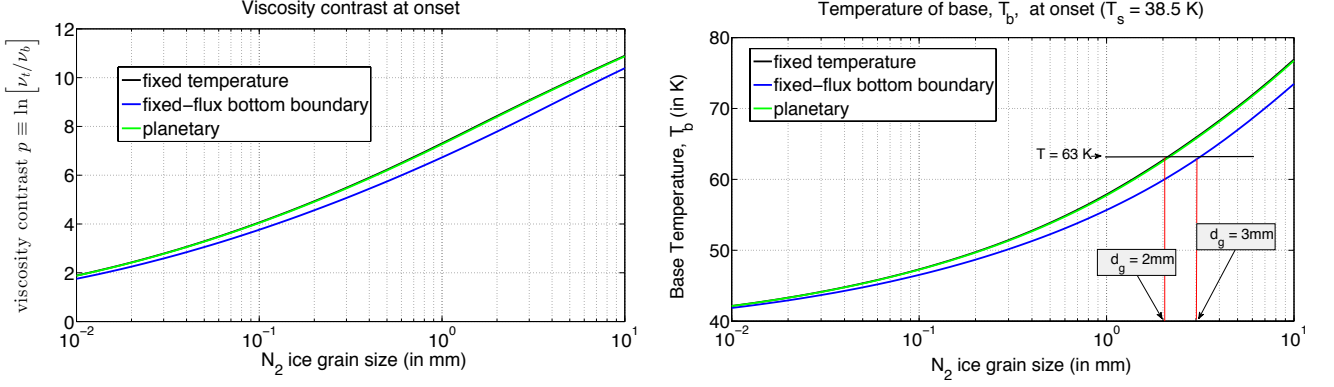


Figure 6: (Left panel) Base temperature at transition into buoyant convection. (Right panel) Viscosity contrast for the onset of convection. Results shown in both panels assessed for parameters shown in Fig. 5. The grain-size values corresponding to melt temperatures at the triple-point for N_2 are designated $d_g \approx 2\text{mm}$ for fixed-temperature and planetary thermal boundary conditions at the base while $d_g \approx 3\text{mm}$ for fixed-flux bottom boundaries.

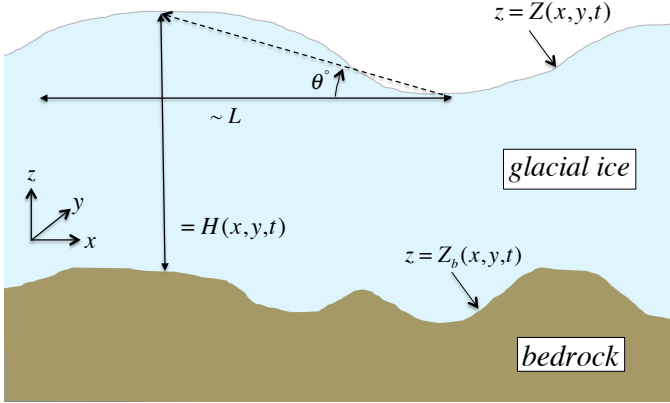


Figure 7: Glacial ice modeling schematic. Evolving glacial ice of thickness $H(x, y, t)$ with surface elevation position $z = Z(x, y, t)$ and bedrock surface $z = Z_b(x, y, t)$. All quantities are space and time dependent. The angle θ describes the grade of the surface feature with horizontal scale $\sim L$.

The dry component of the mass-flux coefficient is given by

$$q_{\text{dry}} = g_{\mathcal{Q}} \exp \left[\frac{H/H_a}{1 + H/H_{\Delta T}} \right] q_{\text{glen}},$$

$$q_{\text{glen}} \equiv \frac{A_s (\rho_s g H)^n H^2}{n + 2} S^{n-1}. \quad (14)$$

The model adopts a non-Newtonian Glen law formulation (Section 2.2) modified to take into account the strongly insulating nature of nitrogen ice (Section 2.1). The classical Glen law part of the expression is contained in q_{glen} where the Glen law index is n . S is the local scalar tangent of the surface, i.e., $S \equiv |\nabla Z|$. $A_s = A(T_s)$ is the value of the Arrhenius prefactor expression, found in equation (2), evaluated at the surface temperature T_s . The parameters appearing in the dry glacial mass flux formula, equation (15), H_a and $H_{\Delta T}$, are given by

$$H_{\Delta T} = T_s / \bar{T}_{0z}, \quad H_a = T_s^2 / (T_a \bar{T}_{0z}),$$

where T_a, \bar{T}_{0z} are respectively, the activation temperature of N_2 ice (Section 2.1) and the vertical temperature gradient inside the ice (Section 2.3). The order 1 numerical parameter $g_{\mathcal{Q}}$, which is a corrective term depending upon the rheology of the flowing material, is described in detail in Appendix C. For all of our subsequent modeling we adopt a constant value of $g_{\mathcal{Q}} = 0.5$.

The mass flux coefficient of the basal sliding component is given by

$$q_{sl} = \frac{H}{|\nabla Z|} \begin{cases} u_{s10}, & H > H_m, \\ \mathbf{0}, & 0 < H < H_m. \end{cases} \quad (15)$$

The physical meaning of the model is that once a minimum thickness H_m is achieved, the base of the layer experiences melt. H_m generally depends upon many physical inputs including latitude, local sloping angle of the surface and the emergent geothermal flux (i.e., \bar{T}_{0z}), but for our purposes in this study we adopt a constant value for it. The wet base adds a constant velocity $u_{s10} \hat{\mathbf{t}}$ to the flowing

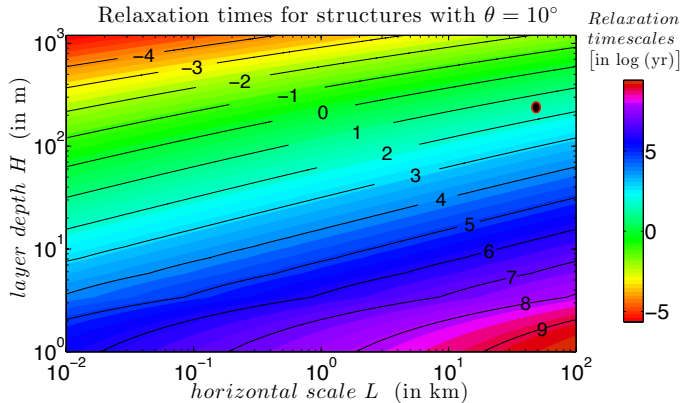


Figure 8: Flow timescales τ for glacial ice structures composed of N_2 ice characterized by the rheology of [20]: glacial ice configurations with surface sloping grades of $\theta = 10^\circ$. Flow timescales are presented for a range of horizontal and layer-depths L and H respectively. The surface temperature of the ice is $T_s = 38.5\text{K}$ with a vertical temperature gradient $T_{0z} = 20\text{K/km}$. Other parameters are $n = 2.1$, $H_a \approx 175\text{m}$, $H_{\Delta T} = 1925\text{m}$ with $g_Q = 0.5$.

glacier, where $\hat{\mathbf{t}} \equiv \nabla Z / |\nabla Z|$ is a unit vector indicating the map-projected direction of the local downslope of the ice. The speed u_{s10} is the magnitude of the basal flow which we treat as a model input parameter, but it may generally be considered to be a function of other inputs like total overburden pressure and temperature. This physical model is derived from terrestrial glacial flow modeling⁶.

We reflect upon the functional dependence on the dry mass-flux coefficient q_{dry} , which scales as

$$\sim H^{n+2} \exp\left(\frac{H/H_a}{1 + H/H_{\Delta T}}\right),$$

indicating its significant deviation from the classical Glen Law form used for terrestrial glacial ice modeling, i.e., the classical form contained in the expression q_{glen} . We refer to this composite form as the Arrhenius-Glen mass-flux dependency. This new form reflects the Arrhenius prefactor of N_2 's rheology, which becomes significant because of the strongly insulating nature of N_2 that promotes the development of strong temperature gradients inside a conducting layer of N_2 ice. This occurs on a relatively short period of time (see discussion in Section 2.3).

5. Some model results

We present here a preliminary examination of the two questions/scenarios posed in the Introduction. We work

⁶ Caution is advised. It is likely that a basally wet N_2 ice layer may behave differently than basally wet terrestrial H_2O ice glaciers owing primarily to the lower density of liquid N_2 compared to its solid phase. Sufficiently thick layers of low viscosity liquid N_2 underneath an ice layer should lead to Rayleigh-Taylor instabilities which would, consequently, lead to vertical mixing of the liquid N_2 with the overlaying ice. Further theory is required in this instance.

with model landscapes adapted from digital elevation models (DEM) of two regions on the eastern side of SP (further detailed below in section 5.2). We treat these surfaces as the primary bedrock and onto them we add a certain amount of N_2 ice and observe the response. We solve eqs. (12-15) using a stripped down version of MARSSIM [36] in which the glacial flow law is assessed using both either a second or fourth order correct finite-difference flux method. The program solves the equations of motion in a doubly periodic domain.

5.1. Flow timescales - some estimates

We can make certain estimates regarding the flow timescales associated with various ice-configurations assuming dry N_2 ice layers. We adopt the rheology of [20] – but we keep in mind that all estimates made here will need to be revised when future improvements to N_2 ice's rheology are made available.

An e-folding flow timescale, τ , may be assigned to surface features of horizontal length L , vertical height H , and surface gradients characterized by the grade angle θ . Assuming that the bedrock is static, temporal variations in Z are the same as temporal variations in H . Thus, the left hand side of the evolution equation (12) may be approximated by H/τ . Using the form for the mass-flux given by Eq. (13) together with the approximate form for the dry N_2 ice mass-flux q_{dry} in eq. (14), and the assumption that horizontal variations of surface features scale with L (see Fig. 7), the order-of-magnitude measure of the right-hand-side of Eq. (12) is given by $\sim L^{-1}|q_0 \tan \theta|$. Putting these two estimates together produces the following expression for the rate τ^{-1} ,

$$\begin{aligned} \tau^{-1} &\approx \frac{|q_0 \tan \theta|}{HL}, \\ &= g_Q \frac{H A_s (\rho_s g H)^n}{L (n+2)} \exp\left[\frac{H/H_a}{1 + H/H_{\Delta T}}\right] |\tan \theta|^n. \end{aligned} \quad (16)$$

We note that as written, L/τ approximates the surface velocity of the flowing glacier ice. In Figures 8-9 we present color contour plots for the relaxation times associated with a variety of glacial structures with various values of H , L and θ (see Fig. 7).

Some noteworthy figures emerge. The black oval in Figure 8 designates the e-folding relaxation time associated with a 50km long channel, sloping at $\theta = 10^\circ$ and initiated with 200 m of glacial ice. The corresponding relaxation time is about 50 years, similar to the figure reported in [2]. One may interpret this time-frame equivalently as the e-folding period on which such a channel drains out a $(1 - 1/e)$ fraction of its initial ice content. Imagining that we indeed begin with 200 m N_2 thick layer and after the just described e-folding timescale, we would have remaining an ice layer of about 75 m thick which, according to Figure 8, ought to undergo another $(1 - 1/e)$ fractional drain in about 5000 years. Of course, this difference in drainage times is due to the strong nonlinear

dependence of the mass-flux on H , namely the Arrhenius functional dependence shown in Eq. (14). Nonetheless, and all other things being equal (especially the surface temperature T_s), any substantial amounts of ice accumulated in such drainage channels are likely to drain out to levels (say, below 50 meters) in well under 100-500 years ($\sim 0.5 - 2$ Plutonian orbits). Similar timescale estimates can be made for structures and channels of differing extents and depths.

5.2. Sample initial surfaces from digital elevation models

As we are interested in the character of N_2 ice flow on Pluto, we have adopted two regions along the eastern shoreline of SP to use as the topography on which the glacial ice flows. These two rectangular regions called GL-1 and GL-2, the locations with respect to SP of which are indicated in Figure 3, are extracted from DEMs created using stereogrammetry – a method of elevation determination applied successfully in many previous studies focusing on icy satellites [37, 38]. The master stereo DEM was created from 0.495 and 0.32 km/px observations⁷ – both of which are observations obtained using the MVIC camera. The pixel scale we adopt therefore is 0.495 km/px. The precision in relief for these DEMs is about 225 meters [2].

The initial bedrock landscapes used in our simulations, shown in Figure 10, are primed for use based on the following procedure. Because the stripped-down version of MARSSIM we use solves the equations of motion in a doubly periodic domain, the landscape should have equal elevations and gradients along the borders of the computational domain. We therefore take the raw DEM, $Z_{\text{raw}}(x, y)$ and apply a filter which forces the elevation to be equal along the borders of the rectangular section as well as forcing the gradients there to be zero. We simultaneously impose a minimum elevation requirement at some arbitrary level Z_{min} , i.e.

$$Z_{\text{raw}} \rightarrow Z_{\text{b}} = \max[Z_{\text{raw}}, Z_{\text{min}}].$$

We always choose the elevation on the computational border to be equal to the minimum elevation Z_{min} . The resulting landscape looks like an island as can be seen in the figures. The choice of Z_{min} is guided by our desire to have some interesting topographic features appearing along the shoreline of these island-like landscapes (like, for instance, the topography indicated by red arrows on the top panel of Fig. 10). The final stage involves doubling the resolution of the model landscape using a third order spline method. This is done in order to smooth out small (pixel to pixel) scale scatter that is a byproduct of most DEM methods including stereogrammetry. [37, 38]. The grid resolution of each of the two landscapes GL-1 and GL-2 are respectively, $N_x \times N_y = 304 \times 340, 424 \times 452$.

⁷Specifically, these are the P_MPAN1 observation (resolution 0.495 km/px) and the P_MVIC_LORRI_CA observation (resolution 0.32 km/px).

5.3. Some numerical results

We discuss here three suites of solutions. Each landform evolution simulation begins with a mound of N_2 ice centered on at the map position $(x, y) = (x_c, y_c)$, with a form given by

$$H_0 = H_{r_0} \exp \left[\left(\frac{r}{\delta r} \right)^m \right], \quad (17)$$

where $r = \sqrt{(x - x_c)^2 + (y - y_c)^2}$. All initial profiles use a power index $m = 6$. The resulting profile looks like an inverted dinner plate where ice regions close to $r = 0$ are nearly flat with thickness H_{r_0} , while a precipitous drop off occurs at the value of r approaching the nominal mound size, δr . All numerical simulations adopt the non-Newtonian Arrhenius ice rheology of annealed N_2 [20]. Thus, for q_{dry} , we use the formula eq. (14), wherein we adopt the ice surface temperatures to be $T_s = 38.5\text{K}$, together with $\bar{T}_{0z} = 20\text{K/km}$ and $T_a = 425\text{K}$ – which taken together leads to $H_a = 0.175\text{km}$ and $H_{\Delta T} = 1.95\text{km}$.

Figure 11 displays the results of a numerical simulation in which the initial N_2 ice mound with $\delta r = 4.3\text{km}$ is emplaced in the highlands of landscape GL-1 ($x_c = 3\text{km}$, $y_c = -4\text{km}$), with a very large ice thickness $H_{r_0} = 0.7\text{km}$. Despite the large value of H_{r_0} , the layer is evolved as a dry glacier (i.e. no basal melting) because the purpose of this demonstration is to exhibit how flowing glacial ice reflects bottom topography. After an initial adjustment phase of this advancing dry glacier ($< 1\text{yr}$),⁸ significant ice drainage from the uplands and onto the flats occurs in under 10-20 years – both timescales which are consistent with the glacial timescale calculation in section 5.1 as well as the numbers quoted in [2].

There are several notable features in the results. Most prominently is how the ridge-line indicated by the large arrow in Fig.10 is clearly imprinted on the surface ice once it has covered the ridgeline. The dark elongate feature in Fig. 11c, that is cut by the white transect arrow, is the expression of the aforementioned ridgeline. This elongated feature on the surface ice indicates a drop in the ice level of about 10-20 meters as can be seen in Fig. 11e. Physically speaking, this drop in the ice level at the 8km mark along this transect indicates the effect of ice piling up as it moves over and around the subsurface ridge. There are other similar elongated dark features that also similarly reflect short lengthscale changes in the bottom topography (yellow arrow). By late times, $t = 489\text{yrs}$ Fig. 11d, this

⁸All numerical simulations performed here have been initiated with relatively “unnatural” initial ice distributions, in the sense that they represent ice accumulations that are not those realizable from some quasi-steady process. As such, in all such cases, the simulations go through two typical stages: (i) a rapid initial readjustment phase followed by a (ii) slower creeping relaxation stage. In order to avoid numerical instabilities, this initial rapid readjustment phase must be evolved with relatively small time steps. After a sufficient amount of time in which the slowly creeping relaxation phase is reached, the time-stepping of the simulations may then be increased – generally by a factor of 5-10 times the initial time step.

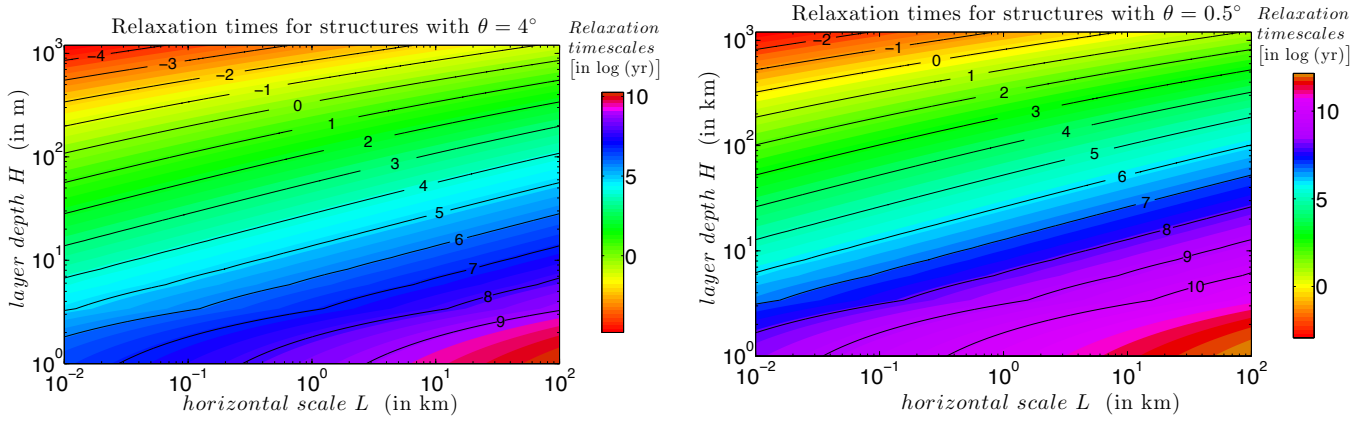


Figure 9: Like Figure 8 except for ice configurations with surface sloping grades of $\theta = 4^\circ$ (top panel) and $\theta = 0.5^\circ$ (bottom panel).

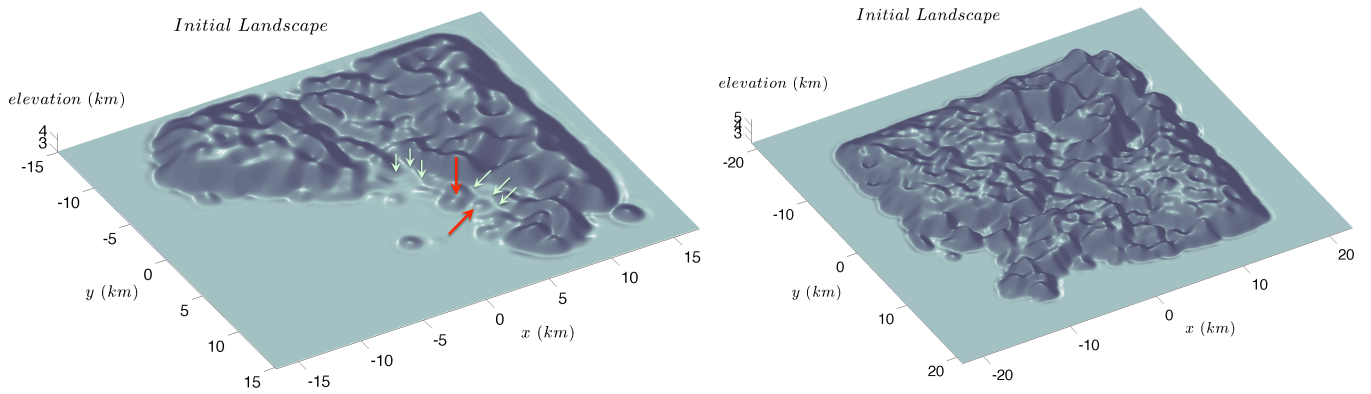


Figure 10: Digital elevation models of two eastern sections of SP called GL-1 (left panel) and GL-2 (right panel). The topography has been artificially flattened along borders of frame to facilitate modeling. This surface is treated as the bedrock upon which we examine various glacial flow responses. Reference topography is indicated for GL-1: local highs (red arrows) and lows (lime arrows). This depiction of the topography simulates lighting coming from the top left of both images.

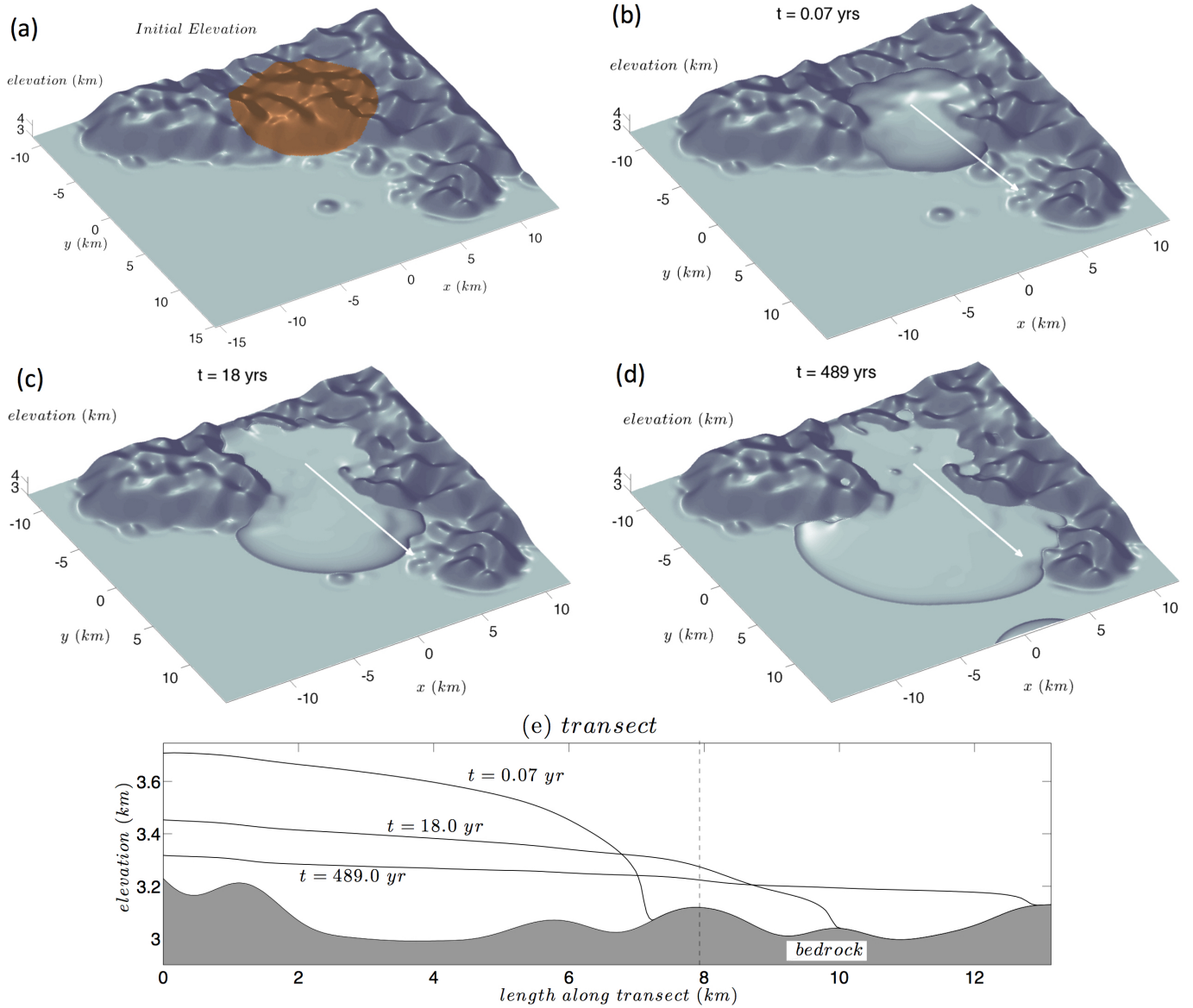


Figure 11: Glacial flow evolution of dry N_2 ice over landscape GL-1 with power law coefficient $n = 2.1$ and initial mound amplitude of $H_{r0} = 0.7$ km. Panel (a) shows initial N_2 ice distribution designated by orange highlight. Panel (b) shows early readjustment of initial configuration ($t = 0.07$ yrs). Panel (c) and (d) show the late time development of the elevation as glacial flows over topography. Flow over topography is especially pronounced over the ridgeline indicated by the red arrow in left panel of Fig. 10 and at transect position ~ 8.0 km in panel (e). By late times ($t = 489$ yrs), the drop in elevation diminishes and the imprint due to the ridgeline topography becomes increasingly imperceptible.

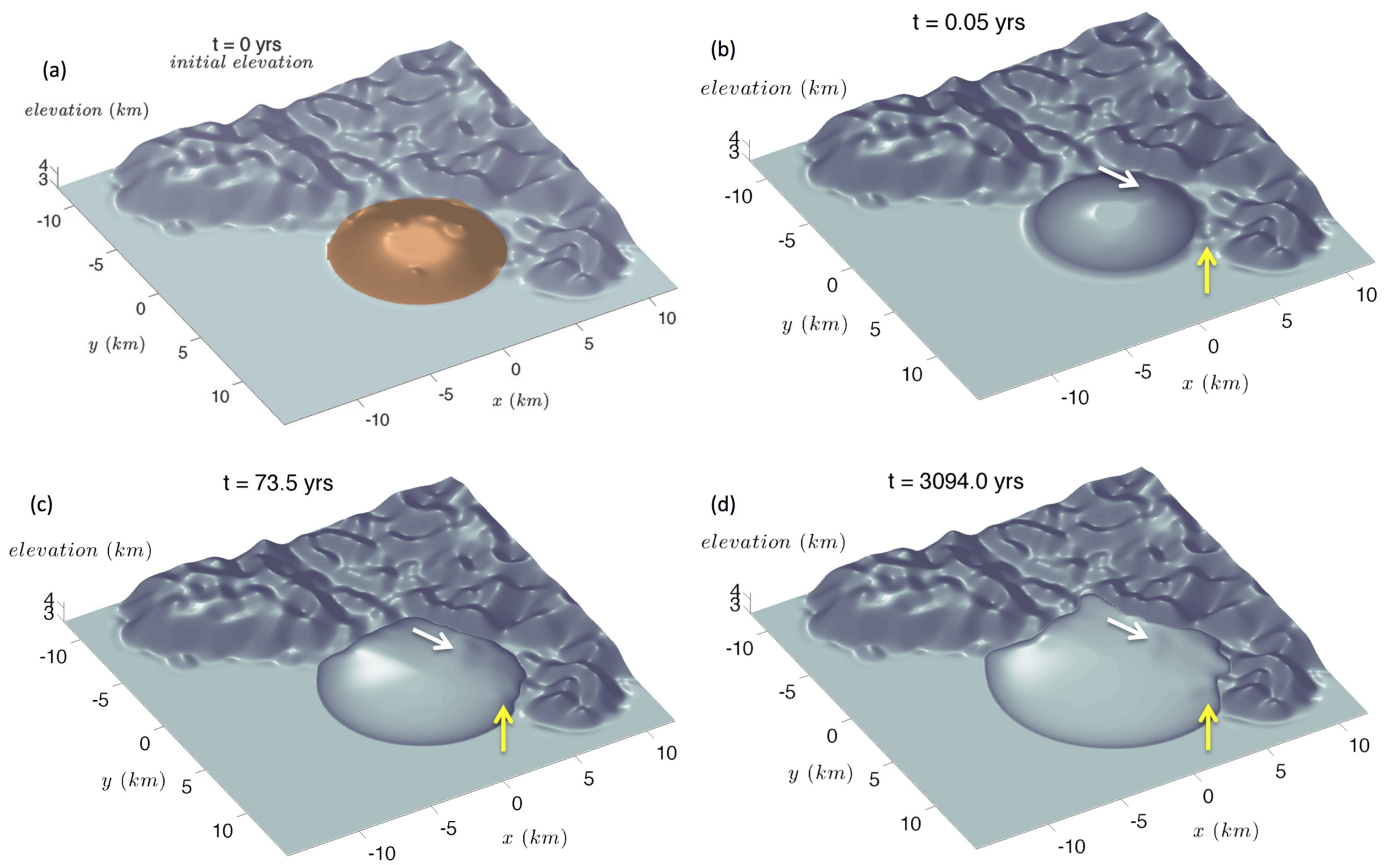


Figure 12: Glacial flow evolution of dry N_2 ice toward landscape GL-1. Flow parameters are $n = 2.1$ and $H_{\Delta T} = 1.95\text{km}$ and $H_a = 0.175\text{km}$ with an initial mound amplitude of $H_{r,0} = 0.7\text{km}$. Panel (a): Initial ice mound emplaced on flat part of bedrock (indicated by orange) is allowed to relax. Panel (b-d): early and late time configurations of this relaxation process. Topographical imprint upon the flowing glacier is apparent (white and yellow arrows). The imprint is relatively weak for this rheology.

surface feature weakens because the drop in the ice level reduces the imprint to nearly imperceptible amounts.

These trends suggest that the wavy elongated features seen on the northern shores of SP, especially those seen in Fig. 2b, are not only imprints of bottom topography but are ephemeral as well. We note here that the imprint is relatively diffuse and this is likely because of the more fluid-like quality of this material due to its low value of the power law index n (see below). Nevertheless, if the wavy darkened features seen near the northern shoreline of SP are indeed imprints of topography, then this zone may have experienced a recent surge of glacial activity (in the last few hundred years). Despite the more fluid-like nature of the ice, the advancing glacial front, descending from the pitted highlands and passing through the basin and out onto the flats of the plain, is reminiscent of terrestrial glaciers that have power law indices closer to the range of $n = 4 - 6$.

Figure 12 displays results of a similar experiment like shown in the previous figure except the original mound is placed on the flat region of landscape GL-1 ($x_c = -2$ km, $y_c = 4$ km) – all other parameters and conditions are otherwise the same. In this instance the flow moves toward the shoreline, yet we see similar qualitative features of topographic imprinting on the moving ice as it begins to envelope exposed relief. Interestingly, the patterning takes on a wavy character once flow begins to move into the mouth of the basin around $x = 0$ km, $y = 0$ km. The wavy feature reflects the local topographic low of the hills in the mouth of the basin – as pointed out by the green arrows in the left panel of Fig. 10. As before, both the wavy features eventually disappear as the N_2 ice flattens out over time and the relief of the topography imprinted upon the ice is fairly muted.

By contrast, in Figure 13 we show the result of a similar setup but with a relatively stiff rheology based on a quadri-Bingham flow model used in describing the features on the surface of Helene [39]. The purpose of this particular demonstration is to show that the wavy features indicating bottom topography are brought out in starker relief for surface flow models with stiffer rheology. The long time fate is the same: the wavy features eventually fade over time as the surface ice relaxes. The actual properties of N_2 ice rheology, possibly contaminated by other pollutants like CH_4 and tholins, remain to be constrained.

We also note the persistence of the curious mesa-looking like feature in the center of the original ice mound in both Figures 12 and 13. This is an artifact introduced by the inverted dinner-plate ice distribution. Because the center of the mound is nearly flat there is hardly any ice movement there initially. It is only when the relaxation front that proceeds from the outer rim works its way back toward the center of the mound does the flatness of the original distribution get modified. The non-circular quality at later times is an expected feature because the flat region upon which the ice mound was emplaced actually has some to-

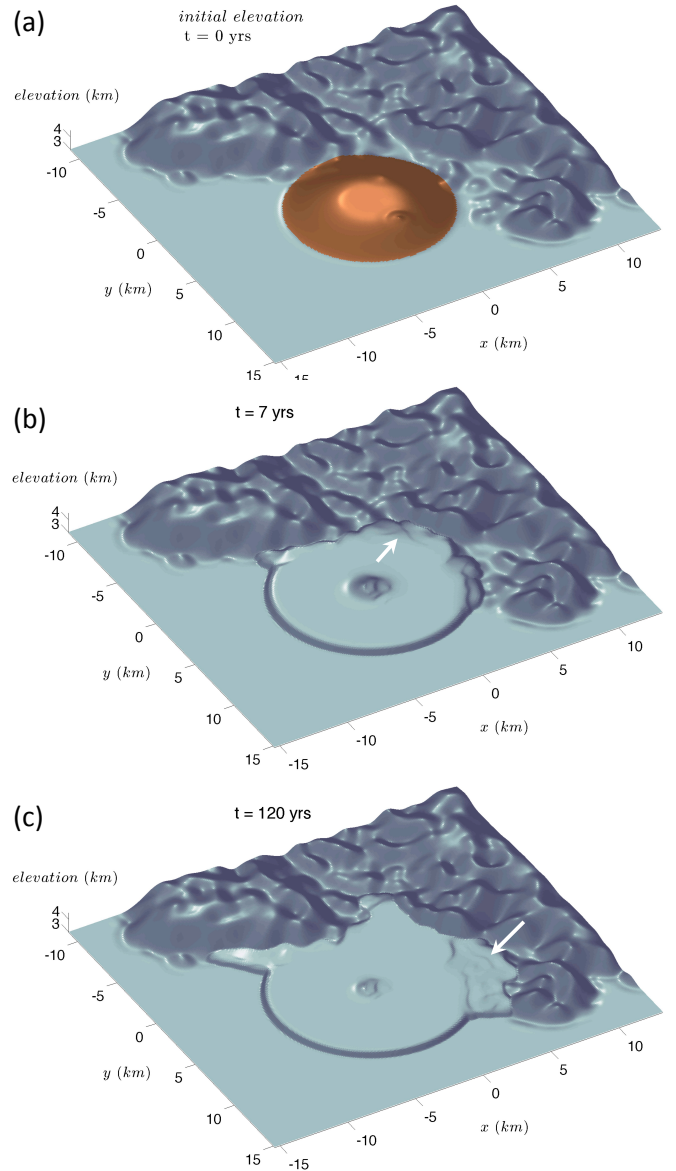


Figure 13: Glacial flow evolution of dry N_2 ice toward landscape GL-1. Similar numerical experiment to Figure 12 except for a stiffer rheology (see text). Panel (b-c): early and late time configurations of this relaxation process. Note the appearance of wavy patterns (white arrows) and their qualitative resemblance to similar undulating patterns seen near the northern shore of SP (Fig. 2). Wavy patterning is an imprint of local topographic extremes shown by the green arrows in the left panel of Fig. 10. The wavy pattern indicated by arrow in panel (b) is no longer visible at later times, panel (c).

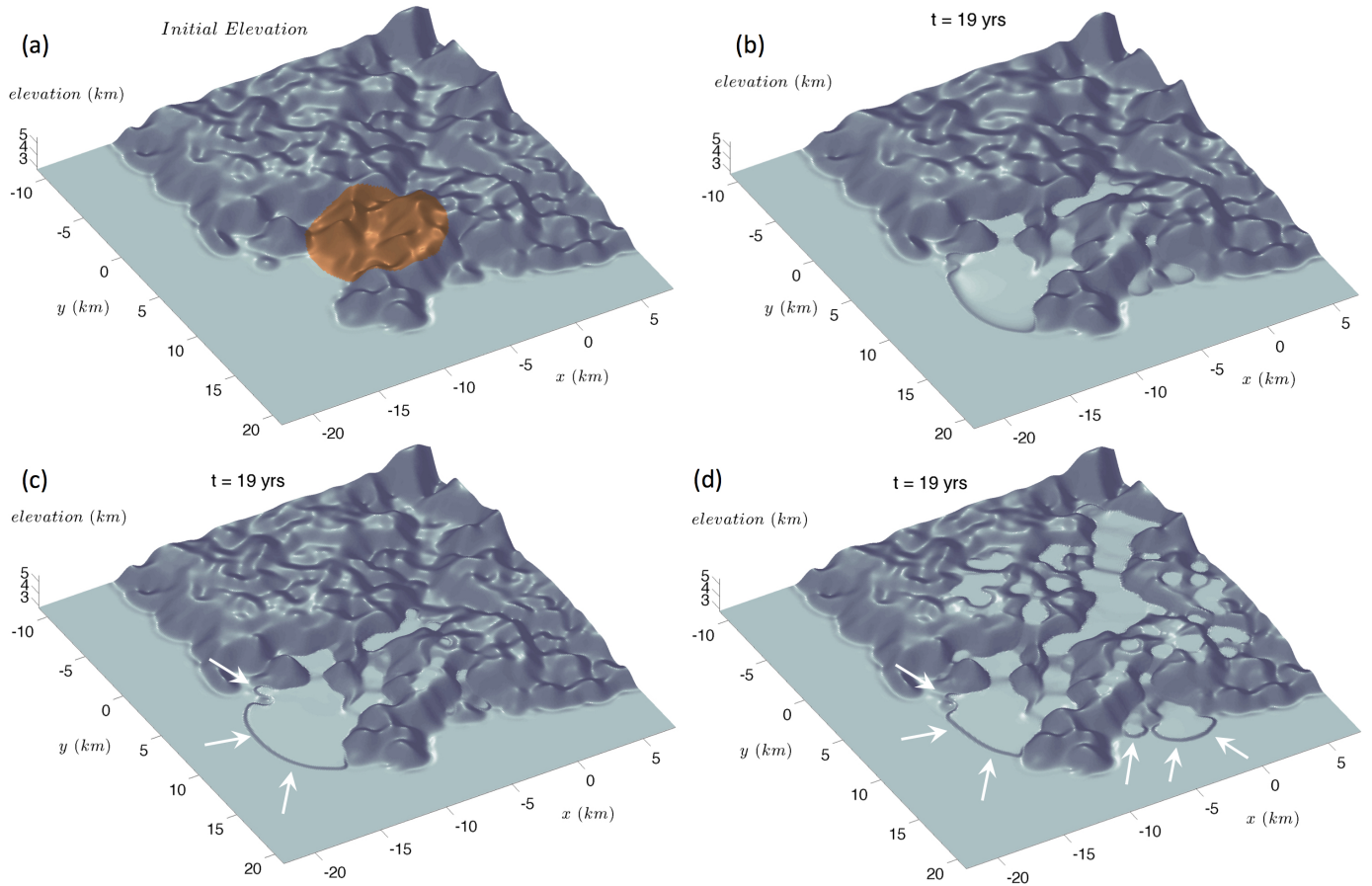


Figure 14: Glacial flow evolution over landscape GL-2 of either basally wet or dry N_2 ice with $n = 2.1$ and $H_{\Delta T} = 1.95\text{km}$ and $H_a = 0.175\text{km}$ and initial mound amplitude of $H_{r,0} = 0.21\text{km}$. Panel (a) exhibits the initial ice mound emplaced on sloping highlands which is then allowed to relax. The resulting shape after 19 years is shown for the case of no basal slip, panel (b); and with basal slip, panel (c). In the latter - slip occurs with a speed $u_{s10} = 0.2\text{km/yr}$ once the local ice layer thickness exceeds $H > H_m = 100\text{m}$. Panel (d) depicts a similar numerical experiment involving basally wet glacial flow, but for a wider shallower initial ice mound (details in text). Owing to the relatively low power law index, simulations of both of basally wet and dry glacial flow develop classical flow lobe features once ice has reached the flats. Flow lobes are more pronounced in basally wet flow simulations. The numerical experiment in panel (d) shows how glacial ice collects inside local topographic lows as well.

pography in its vicinity (see the corresponding location in the left panel of Fig. 10) – the ice flow that ensues is affected by this relief and, consequently, must move around it and locally piles up along the local subsurface relief just as one expects in classical viscous flow around an obstacle.

Figure 14 shows comparative qualitative results involving numerical experiments of both basally wet and dry glaciers advancing on landscape GL-2. Figures 14b-c show the response of an initial ice mound placed on the sloping highlands of GL-2, ($x_c = -7\text{km}$, $y_c = 7\text{km}$) with $\delta r = 4.5\text{km}$ and $H_{r_0} = 0.21\text{km}$ (Figure 14a). Figure 14b shows the resulting flow shape when the simulation is run for 19 years in which the glacial ice is dry. The results are very similar to the developed glacial front shown in Fig. 11. A dry glacier dynamically evolving with this value of $n = 2.1$, which means it leaks like a fluid down gradient, the advancing front weakly exhibits flow lobes upon reaching the flat plains.

Interestingly, Figure 14c shows the result of the same initial configuration except for the difference that the glacial ice is allowed to be wet. In our model, a flowing glacier is considered basally wet (i.e., $q_{sl} \neq 0$), if the layer thickness of the ice H exceeds the critical value for melt at the base which, here, is when $H > H_m = 100\text{m}$. This number is chosen to be consistent with the depth at which melt might occur if the surface temperatures get as high as 57 K (see discussion in section 3). Then according to equation (15), the base of the ice layer will slide downslope with a speed u_{s10} , a value which we have set to 0.2km/yr , a number adopted from basally wet glacier modeling for the Earth [40]. After 19 years, the ice has flown out onto the plains exhibiting more pronounced flow lobe structure – qualitatively reminiscent of the lobate features observed in the New Horizons LORRI image shown in Fig. 1.

Figure 14d shows the result of a similar simulation except the initial ice profile is centered further up the landscape ($x_c = -3\text{km}$, $y_c = 3\text{km}$), with a wider cover ($\delta r = 9.1\text{km}$) and with a shallower thickness ($H_{r_0} = 0.15\text{km}$). The results are similar except that we see fast moving glacial flow reaching the flats and forming tongue-like depositional patterns below from several locations. Also, with a wider initial cover, a significant fraction of the ice rapidly infills local topographic lows. In the particular simulation shown, N_2 ice is still making its way out of the pitted highlands.

6. Summary discussion

In this study we have developed a framework for modeling N_2 glacial ice and we have used it to answer two broad qualitative questions regarding the observations of present-day glacial flow observed on the surface of Pluto. The glacial model incorporates the known published thermophysical properties of solid N_2 . The current-day major uncertainty of the mathematical model is in the rheological properties of N_2 ice under the extreme conditions

of Pluto’s surface. Once more laboratory and theoretical studies regarding N_2 ’s rheology are published, the inputs of the model developed here will need to be updated accordingly. However, the overarching mathematical framework presented here should remain largely unchanged once updates to the rheology are determined.

Our glacial flow model assumes the aspect ratio of the flowing ice is very low, which permits the development of a vertically integrated mathematical formulation (SSA). A low aspect ratio means that one may reasonably assume the ice flows laminae. Thus, an important caveat in using this thin-layer laminar N_2 flow model is the assumption that the layers are not thick enough for N_2 ice to undergo convection, which would violate the assumption of laminar flow. Questions regarding onset, of course, are subject to the uncertainties in the rheology of N_2 ice – a matter which needs further laboratory work to clarify.

As such and as one of the results of this work, we have analyzed the conditions for the onset of convection for a variety of *basal* thermal boundary conditions and find that it should occur for layers whose thicknesses are greater than 300-1000m. This figure that depends upon the N_2 ice grain diameter, whose size distribution is not currently known for the observed N_2 on Pluto, although upper bounds of 1-10 cms have been assessed from analysis of spectroscopic data taken with the LEISA instrument [4]. The thermal boundary conditions considered in our analysis include fixed-temperature conditions (traditional), fixed-flux, and so-called planetary conditions at the base of the convecting layer. The latter two of these boundary conditions, which have not been heretofore examined in the literature in the context of solid-state convection, are meant to represent the thermo-physical conditions at the interface of a passively conducting static bedrock with an overlying N_2 ice layer. We report that the conditions for onset when these latter two boundary conditions are assumed are largely similar to those assessed for the more traditional fixed-temperature basal conditions [41, 6].

The mathematical formulation constructed here also permits the distinction between basally wet and dry glacial flow. In a work appearing in this volume (Earle et al., 2017, this volume), obliquity and orbital precession variations of Pluto can give rise to periods of time in which Pluto’s surface temperature might periodically get as high as 55-60 K for 20-30 year stretches of time. Under such conditions, the base of N_2 ice layers as thin as 100-200 meters can melt, which would mean that one should consider a sliding N_2 layer as a “basally wet glacier” [34, 40]. While the physical manifestation of sliding N_2 melt at the base of its solid ice phase has neither been observed (i.e., either in the laboratory or in images) nor considered much from a theoretical eye, it is reasonable to assume that this can happen for Plutonic N_2 ices. We have both followed and implemented into our model the formulation for basally wet glacier flow used commonly in the terrestrial (water) glaciers literature, e.g., as found in [40]. Given the liquid-solid phase differences between the molecules, we are cau-

tioned from making firm statements based on the basally wet glacier runs we have reported here, although we do feel that the gross qualitative trends seen in our simulations are likely to be robust. As such, when laboratory investigations relevant to both wet and basally wet N₂ glaciers are performed in the future, their results should inform upon improvements to the way in which such sliding masses are modeled and, moreover, much of the basally wet glacier simulations reported here ought be redone.

The vertically integrated glacial flow has a dry mass-flux form that is similar to the more familiar Glen-law formulation, which has a power law dependence with layer thickness, i.e., $\sim H^{n+2}$. However, based on the strongly insulating nature of N₂ ice, we find that the mass-flux formulation deviates from this more traditional form and instead has (what we have here called) an ‘‘Arrhenius-Glen’’ form in which the layer thickness dependence of the mass-flux coefficient is as follows

$$\sim H^{n+2} \exp \left[\frac{H/H_a}{1 + H/H_{\Delta T}} \right],$$

where the parameters H_a and $H_{\Delta T}$ depend upon the activation energy of N₂ ice, the surface temperature of the glacier, and the geothermal flux emerging from the interior of the planet. We are cautioned by noting that future improvements in the knowledge of N₂ ice rheology will likely require reconsideration of the mathematical forms and timescales we have presented in this study.

We have applied this model to qualitatively answer the two questions we have posed in the introduction:

1. The wavy transverse light-dark patterning very near the northern shore of SP (Fig. 2a-b) has been interpreted by us to be evidence of glacial flow from the center of SP toward the shoreline (Howard et al., 2017, this volume). Is the pattern a result of northward advection downwelling zones of convecting N₂ ice or are they imprints of the bottom topography present not too far beneath under the surface? We find from our simulations that it is likely that the features are steps in the flowing N₂ ice tracing out locations of bottom topography. In many simulations that we have run, the darkened features correspond to 10-20 m step drops in the ice level as it passes over the peak of the bottom topography. If the surface ice on Pluto is characterized somehow by a stiffer rheology, perhaps due to contaminants like small CH₄ grains, our simulations indicate that the imprint of bottom topography is more dramatic. Given the currently poor constraints on N₂ ice (and its mixtures), we consider this possibility as not being necessarily ruled out. For stiffer rheologies, the wavy patterns appearing on the surface of the modeled ice can be an indicator of localized lows in the bottom topography. In either case of stiff or non-stiff rheologies, the features are ephemeral as they eventually fade away on time scales approaching a few decades to hundreds of years. If indeed the wavy patterning seen

near the northern shoreline of SP is an indicator of bottom topography, then it is reasonable to suggest that this part of SP has recently experienced a surge of northward flow within the last two centuries – perhaps even as recently as in the last few decades.

2. The dark lobate depositional features seen on the eastern shoreline of SP (Fig. 1) are another strong line of evidence pointing at recent glacial flow activity. Figure 1 shows such glacial flow emanating from the pitted highlands of ETR and onto the flats below. Were the glacial flow events responsible for these and similar features a result of dry or basally wet glacial flow? Our simulations suggest that it is very hard to get *very pronounced* tongue-like lobate features of down-flowing glacial ice if it moves strictly as a dry glacier with a power-law index n around 2. In the simulations we have reported here, the advancing dry glaciers generally form weakly lobate fronts. However, if the base of the glacial ice is wet, then it drains out onto the flats below, exhibiting unmistakably pronounced lobate features like pointed out in Figs. 14c-d.

We are not implying that all N₂ glacial ice that drains into SP from the pitted highlands surrounding SP does so as a wet or basally wet glacier. However, based on the obliquity-eccentricity variations experienced by Pluto, we consider it perhaps possible that there may have been episodes of rapid drainage of the N₂ ice found in the pitted highlands of ETR and into SP when the surface temperatures get high enough, since it would mean basal melt N₂ ice can occur for shallower layer thicknesses. In other words, N₂ ice which would have otherwise emptied into SP’s basin as a dry glacier may have rapidly drained into the basin as a basally wet glacier during these brief periods of surface warming. As a basally wet glacier, then, they could be the origins of the tongue-like lobate features observed on today’s surface. Of course, we caution that these hypothetical possibilities have not yet been assessed to their fullest.

The questions posed and the answers given in this study are very preliminary. When the rheology of N₂ ice, both as a pure substance as well as an ice comprised as a mixture of other volatile grains like CH₄ and CO, most of the simulations and questions examined here must be revisited. Similarly, there are many more questions to be answered at this early stage of discovery. The qualitative ones we have addressed here give us confidence that the glacial model we have developed may be used to answer more detailed and refined questions once more data analysis of Pluto’s surface is complete. One of the next directions is to apply the machinery developed here to answer questions about Pluto’s past glaciation (Howard et al., 2017, this volume).

7. Acknowledgements

The corresponding author thanks Magda Saina for assistance with some of the figures presented here. The authors thank both the anonymous referee as well as Dr. D. A. Patthoff for very helpful suggestions that helped to streamline this work. The authors are also indebted to Dr. W. Grundy for spirited conversations regarding the granular nature of Pluto's surface ices. This work was supported by both NASA's Senior NPP program and NASA's New Horizons project.

8. References

References

- [1] S. A. Stern, F. Bagenal, K. Ennico, G. R. Gladstone, W. M. Grundy, W. B. McKinnon, J. M. Moore, C. B. Olkin, J. R. Spencer, H. A. Weaver, L. A. Young, T. Andert, J. Andrews, M. Banks, B. Bauer, J. Bauman, O. S. Barnouin, P. Bedini, K. Beisser, R. A. Beyer, S. Bhaskaran, R. P. Binzel, E. Birath, M. Bird, D. J. Bogan, A. Bowman, V. J. Bray, M. Brozovic, C. Bryan, M. R. Buckley, M. W. Buie, B. J. Buratti, S. S. Bushman, A. Calloway, B. Carcich, A. F. Cheng, S. Conard, C. A. Conrad, J. C. Cook, D. P. Cruikshank, O. S. Custodio, C. M. Dalle Ore, C. Deboy, Z. J. B. Dischner, P. Dumont, A. M. Earle, H. A. Elliott, J. Ercol, C. M. Ernst, T. Finley, S. H. Flanigan, G. Fountain, M. J. Freeze, T. Greathouse, J. L. Green, Y. Guo, M. Hahn, D. P. Hamilton, S. A. Hamilton, J. Hanley, A. Harch, H. M. Hart, C. B. Hersman, A. Hill, M. E. Hill, D. P. Hinson, M. E. Holdridge, M. Horanyi, A. D. Howard, C. J. A. Howett, C. Jackman, R. A. Jacobson, D. E. Jennings, J. A. Kammer, H. K. Kang, D. E. Kaufmann, P. Kollmann, S. M. Krimigis, D. Kusnierkiewicz, T. R. Lauer, J. E. Lee, K. L. Lindstrom, I. R. Linscott, C. M. Lisse, A. W. Lunsford, V. A. Mallder, N. Martin, D. J. McComas, R. L. McNutt, D. Mehoke, T. Mehoke, E. D. Melin, M. Mutchler, D. Nelson, F. Nimmo, J. I. Nunez, A. Ocampo, W. M. Owen, M. Paetzold, B. Page, A. H. Parker, J. W. Parker, F. Pelletier, J. Peterson, N. Pinkine, M. Piquette, S. B. Porter, S. B. Porter, S. Protopapa, J. Redfern, H. J. Reitsema, D. C. Reuter, J. H. Roberts, S. J. Robbins, G. Rogers, D. Rose, K. Runyon, K. D. Retherford, M. G. Ryschkewitsch, P. Schenk, E. Schindhelm, B. Sepan, M. R. Showalter, K. N. Singer, M. Soluri, D. Stanbridge, A. J. Steffl, D. F. Strobel, T. Stryk, M. E. Summers, J. R. Szalay, M. Tapley, A. Taylor, H. Taylor, H. B. Throop, C. C. C. Tsang, G. L. Tyler, O. M. Umurhan, A. J. Verbiscer, M. H. Versteeg, M. Vincent, R. Webbert, S. Weidner, G. E. Weigle, O. L. White, K. Whittenburg, B. G. Williams, K. Williams, S. Williams, W. W. Woods, A. M. Zangari, E. Zirnstein, The Pluto system: Initial results from its exploration by New Horizons, *Science* 350 (2015) aad1815. [arXiv:1510.07704](#), [doi:10.1126/science.aad1815](#).
- [2] J. M. Moore, W. B. McKinnon, J. R. Spencer, A. D. Howard, P. M. Schenk, R. A. Beyer, F. Nimmo, K. N. Singer, O. M. Umurhan, O. L. White, S. A. Stern, K. Ennico, C. B. Olkin, H. A. Weaver, L. A. Young, R. P. Binzel, M. W. Buie, B. J. Buratti, A. F. Cheng, D. P. Cruikshank, W. M. Grundy, I. R. Linscott, H. J. Reitsema, D. C. Reuter, M. R. Showalter, V. J. Bray, C. L. Chavez, C. J. A. Howett, T. R. Lauer, C. M. Lisse, A. H. Parker, S. B. Porter, S. J. Robbins, K. Runyon, T. Stryk, H. B. Throop, C. C. C. Tsang, A. J. Verbiscer, A. M. Zangari, A. L. Chaikin, D. E. Wilhelms, F. Bagenal, G. R. Gladstone, T. Andert, J. Andrews, M. Banks, B. Bauer, J. Bauman, O. S. Barnouin, P. Bedini, K. Beisser, S. Bhaskaran, E. Birath, M. Bird, D. J. Bogan, A. Bowman, M. Brozovic, C. Bryan, M. R. Buckley, S. S. Bushman, A. Calloway, B. Carcich, S. Conard, C. A. Conrad, J. C. Cook, O. S. Custodio, C. M. D. Ore, C. Deboy, Z. J. B. Dischner, P. Dumont, A. M. Earle, H. A. Elliott, J. Ercol, C. M. Ernst, T. Finley, S. H. Flanigan, G. Fountain, M. J. Freeze, J. L. Green, Y. Guo, M. Hahn, D. P. Hamilton, S. A. Hamilton, J. Hanley, A. Harch, H. M. Hart, C. B. Hersman, A. Hill, M. E. Hill, M. E. Holdridge, M. Horanyi, A. D. Howard, C. J. A. Howett, C. Jackman, R. A. Jacobson, D. E. Jennings, H. K. Kang, D. E. Kaufmann, P. Kollmann, S. M. Krimigis, D. Kusnierkiewicz, T. R. Lauer, J. E. Lee, K. L. Lindstrom, A. W. Lunsford, V. A. Mallder, N. Martin, D. J. McComas, R. L. McNutt, D. Mehoke, T. Mehoke, E. D. Melin, M. Mutchler, D. Nelson, F. Nimmo, J. I. Nunez, A. Ocampo, W. M. Owen, M. Paetzold, B. Page, F. Pelletier, J. Peterson, N. Pinkine, M. Piquette, S. B. Porter, S. Protopapa, J. Redfern, H. J. Reitsema, D. C. Reuter, J. H. Roberts, S. J. Robbins, G. Rogers, D. Rose, K. Runyon, M. G. Ryschkewitsch, P. Schenk, B. Sepan, M. R. Showalter, M. Soluri, D. Stanbridge, T. Stryk, J. R. Szalay, H. A. Elliott, J. Ercol, C. M. Ernst, T. Finley, S. H. Flanigan, G. Fountain, M. J. Freeze, T. Greathouse, J. L. Green, Y. Guo, M. Hahn, D. P. Hamilton, S. A. Hamilton, J. Hanley, A. Harch, H. M. Hart, C. B. Hersman, A. Hill, M. E. Hill, D. P. Hinson, M. E. Holdridge, M. Horanyi, C. Jackman, R. A. Jacobson, D. E. Jennings, J. A. Kammer, H. K. Kang, D. E. Kaufmann, P. Kollmann, S. M. Krimigis, D. Kusnierkiewicz, J. E. Lee, K. L. Lindstrom, A. W. Lunsford, V. A. Mallder, N. Martin, D. J. McComas, R. L. McNutt, D. Mehoke, T. Mehoke, E. D. Melin, M. Mutchler, D. Nelson, J. I. Nunez, A. Ocampo, W. M. Owen, M. Paetzold, B. Page, J. W. Parker, F. Pelletier, J. Peterson, N. Pinkine, M. Piquette, S. Protopapa, J. Redfern, J. H. Roberts, G. Rogers, D. Rose, K. D. Retherford, M. G. Ryschkewitsch, E. Schindhelm, B. Sepan, M. Soluri, D. Stanbridge, A. J. Steffl, D. F. Strobel, M. E. Summers, J. R. Szalay, M. Tapley, A. Taylor, H. Taylor, G. L. Tyler, M. H. Versteeg, M. Vincent, R. Webbert, S. Weidner, G. E. Weigle, K. Whittenburg, B. G. Williams, K. Williams, S. Williams, W. W. Woods, E. Zirnstein, The geology of Pluto and Charon through the eyes of New Horizons, *Science* 351 (2016) 1284–1293. [arXiv:1604.05702](#), [doi:10.1126/science.aad7055](#).
- [3] D. C. Reuter, S. A. Stern, J. Scherrer, D. E. Jennings, J. W. Baer, J. Hanley, L. Hardaway, A. Lunsford, S. McMuldroch, J. Moore, C. Olkin, R. Parizek, H. Reitsma, D. Sabatke, J. Spencer, J. Stone, H. Throop, J. van Cleve, G. E. Weigle, L. A. Young, Ralph: A Visible/Infrared Imager for the New Horizons Pluto/Kuiper Belt Mission, *Space Science Research* 140 (2008) 129–154. [arXiv:0709.4281](#), [doi:10.1007/s11214-008-9375-7](#).
- [4] W. M. Grundy, R. P. Binzel, B. J. Buratti, J. C. Cook, D. P. Cruikshank, C. M. Dalle Ore, A. M. Earle, K. Ennico, C. J. A. Howett, A. W. Lunsford, C. B. Olkin, A. H. Parker, S. Philippe, S. Protopapa, E. Quirico, D. C. Reuter, B. Schmitt, K. N. Singer, A. J. Verbiscer, R. A. Beyer, M. W. Buie, A. F. Cheng, D. E. Jennings, I. R. Linscott, J. W. Parker, P. M. Schenk, J. R. Spencer, J. A. Stansberry, S. A. Stern, H. B. Throop, C. C. C. Tsang, H. A. Weaver, G. E. Weigle, L. A. Young, Surface compositions across Pluto and Charon, *Science* 351 (2016) aad9189. [doi:10.1126/science.aad9189](#).
- [5] G. R. Gladstone, S. A. Stern, K. Ennico, C. B. Olkin, H. A. Weaver, L. A. Young, M. E. Summers, D. F. Strobel, D. P. Hinson, J. A. Kammer, A. H. Parker, A. J. Steffl, I. R. Linscott, J. W. Parker, A. F. Cheng, D. C. Slater, M. H. Versteeg, T. K. Greathouse, K. D. Retherford, H. Throop, N. J. Cunningham, W. W. Woods, K. N. Singer, C. C. C. Tsang, E. Schindhelm, C. M. Lisse, M. L. Wong, Y. L. Yung, X. Zhu, W. Curdt, P. Lavvas, E. F. Young, G. L. Tyler, F. Bagenal, W. M. Grundy, W. B. McKinnon, J. M. Moore, J. R. Spencer, T. Andert, J. Andrews, M. Banks, B. Bauer, J. Bauman, O. S. Barnouin, P. Bedini, K. Beisser, R. A. Beyer, S. Bhaskaran, R. P. Binzel, E. Birath, M. Bird, D. J. Bogan, A. Bowman, V. J. Bray, M. Brozovic, C. Bryan, M. R. Buckley, M. W. Buie, B. J. Buratti, S. S. Bushman, A. Calloway, B. Carcich, S. Conard, C. A. Conrad, J. C. Cook, D. P. Cruikshank, O. S. Custodio, C. M. D. Ore, C. Deboy, Z. J. B. Dischner, P. Dumont, A. M. Earle, H. A. Elliott, J. Ercol, C. M. Ernst, T. Finley, S. H. Flanigan, G. Fountain, M. J. Freeze, J. L. Green, Y. Guo, M. Hahn, D. P. Hamilton, S. A. Hamilton, J. Hanley, A. Harch, H. M. Hart, C. B. Hersman, A. Hill, M. E. Hill, M. E. Holdridge, M. Horanyi, A. D. Howard, C. J. A. Howett, C. Jackman, R. A. Jacobson, D. E. Jennings, H. K. Kang, D. E. Kaufmann, P. Kollmann, S. M. Krimigis, D. Kusnierkiewicz, T. R. Lauer, J. E. Lee, K. L. Lindstrom, A. W. Lunsford, V. A. Mallder, N. Martin, D. J. McComas, R. L. McNutt, D. Mehoke, T. Mehoke, E. D. Melin, M. Mutchler, D. Nelson, F. Nimmo, J. I. Nunez, A. Ocampo, W. M. Owen, M. Paetzold, B. Page, F. Pelletier, J. Peterson, N. Pinkine, M. Piquette, S. B. Porter, S. Protopapa, J. Redfern, H. J. Reitsema, D. C. Reuter, J. H. Roberts, S. J. Robbins, G. Rogers, D. Rose, K. Runyon, M. G. Ryschkewitsch, P. Schenk, B. Sepan, M. R. Showalter, M. Soluri, D. Stanbridge, T. Stryk, J. R. Szalay, H. A. Elliott, J. Ercol, C. M. Ernst, T. Finley, S. H. Flanigan, G. Fountain, M. J. Freeze, J. L. Green, Y. Guo, M. Hahn, D. P. Hamilton, S. A. Hamilton, J. Hanley, A. Harch, H. M. Hart, C. B. Hersman, A. Hill, M. E. Hill, M. E. Holdridge, M. Horanyi, A. D. Howard, C. J. A. Howett, C. Jackman, R. A. Jacobson, D. E. Jennings, H. K. Kang, D. E. Kaufmann, P. Kollmann, S. M. Krimigis, D. Kusnierkiewicz, T. R. Lauer, J. E. Lee, K. L. Lindstrom, A. W. Lunsford, V. A. Mallder, N. Martin, D. J. McComas, R. L. McNutt, D. Mehoke, T. Mehoke, E. D. Melin, M. Mutchler, D. Nelson, F. Nimmo, J. I. Nunez, A. Ocampo, W. M. Owen, M. Paetzold, B. Page, F. Pelletier, J. Peterson, N. Pinkine, M. Piquette, S. B. Porter, S. Protopapa, J. Redfern, H. J. Reitsema, D. C. Reuter, J. H. Roberts, S. J. Robbins, G. Rogers, D. Rose, K. Runyon, M. G. Ryschkewitsch, P. Schenk, B. Sepan, M. R. Showalter, M. Soluri, D. Stanbridge, T. Stryk, J. R. Szalay, H. A. Elliott, J. Ercol, C. M. Ernst, T. Finley, S. H. Flanigan, G. Fountain, M. J. Freeze, T. Greathouse, J. L. Green, Y. Guo, M. Hahn, D. P. Hamilton, S. A. Hamilton, J. Hanley, A. Harch, H. M. Hart, C. B. Hersman, A. Hill, M. E. Hill, D. P. Hinson, M. E. Holdridge, M. Horanyi, A. D. Howard, C. J. A. Howett, C. Jackman, R. A. Jacobson, D. E. Jennings, J. A. Kammer, H. K. Kang, D. E. Kaufmann, P. Kollmann, S. M. Krimigis, D. Kusnierkiewicz, J. E. Lee, K. L. Lindstrom, A. W. Lunsford, V. A. Mallder, N. Martin, D. J. McComas, R. L. McNutt, D. Mehoke, T. Mehoke, E. D. Melin, M. Mutchler, D. Nelson, J. I. Nunez, A. Ocampo, W. M. Owen, M. Paetzold, B. Page, J. W. Parker, F. Pelletier, J. Peterson, N. Pinkine, M. Piquette, S. Protopapa, J. Redfern, J. H. Roberts, G. Rogers, D. Rose, K. D. Retherford, M. G. Ryschkewitsch, E. Schindhelm, B. Sepan, M. Soluri, D. Stanbridge, A. J. Steffl, D. F. Strobel, M. E. Summers, J. R. Szalay, M. Tapley, A. Taylor, H. Taylor, G. L. Tyler, M. H. Versteeg, M. Vincent, R. Webbert, S. Weidner, G. E. Weigle, K. Whittenburg, B. G. Williams, K. Williams, S. Williams, W. W. Woods, E. Zirnstein, The geology of Pluto and Charon through the eyes of New Horizons, *Science* 351 (2016) aad9189. [doi:10.1126/science.aad9189](#).

- lay, M. Tapley, A. Taylor, H. Taylor, O. M. Umurhan, A. J. Verbiscer, M. H. Versteeg, M. Vincent, R. Webbert, S. Weidner, G. E. Weigle, O. L. White, K. Whittenburg, B. G. Williams, K. Williams, S. Williams, A. M. Zangari, E. Zirnstein, The atmosphere of Pluto as observed by New Horizons, *Science* 351 (2016) aad8866. doi:10.1126/science.aad8866.
- [6] W. B. McKinnon, F. Nimmo, T. Wong, P. M. Schenk, O. L. White, J. H. Roberts, J. M. Moore, J. R. Spencer, A. D. Howard, O. M. Umurhan, S. A. Stern, H. A. Weaver, C. B. Olkin, L. A. Young, K. E. Smith, J. M. Moore, W. B. McKinnon, J. R. Spencer, R. Beyer, M. Buie, B. Buratti, A. Cheng, D. Cruikshank, C. Dalle Ore, R. Gladstone, W. Grundy, A. Howard, T. Lauer, I. Linscott, F. Nimmo, C. Olkin, J. Parker, S. Porter, H. Reitsema, D. Reuter, J. H. Roberts, S. Robbins, P. M. Schenk, M. Showalter, K. Singer, D. Strobel, M. Summers, L. Tyler, H. Weaver, O. L. White, O. M. Umurhan, M. Banks, O. Barnouin, V. Bray, B. Carcich, A. Chaikin, C. Chavez, C. Conrad, D. Hamilton, C. Howett, J. Hofgartner, J. Kammer, C. Lisse, A. Marcotte, A. Parker, K. Retherford, M. Saina, K. Runyon, E. Schindhelm, J. Stansberry, A. Steffl, T. Stryk, H. Throop, C. Tsang, A. Verbiscer, H. Winters, A. Zangari, G. a. I. T. T. New Horizons Geology, Convection in a volatile nitrogen-ice-rich layer drives Pluto's geological vigour, *Nature* 534 (2016) 82–85. doi:10.1038/nature18289.
- [7] W. B. Durham, O. Prieto-Ballesteros, D. L. Goldsby, J. S. Kargel, Rheological and Thermal Properties of Icy Materials, *Space Sci. Rev.* 153 (2010) 273–298. doi:10.1007/s11214-009-9619-1.
- [8] A. D. Howard, J. M. Moore, P. M. Schenk, O. L. White, J. Spencer, Sublimation-driven erosion on Hyperion: Topographic analysis and landform simulation model tests, *Icarus* 220 (2012) 268–276. doi:10.1016/j.icarus.2012.05.013.
- [9] A. M. Earle, R. P. Binzel, Pluto's insolation history: Latitudinal variations and effects on atmospheric pressure, *Icarus* 250 (2015) 405–412. doi:10.1016/j.icarus.2014.12.028.
- [10] A. R. Dobrovolskis, A. W. Harris, The obliquity of Pluto, *Icarus* 55 (1983) 231–235. doi:10.1016/0019-1035(83)90077-5.
- [11] B. Schmitt, C. de Bergh, M. Festou (Eds.), *Solar system ices*, Vol. 227 of *Astrophysics and Space Science Library*, 1998. doi:10.1007/978-94-011-5252-5.
- [12] T. A. Scott, Solid and liquid nitrogen, *Physics Reports* 27 (1976) 89–157. doi:10.1016/0370-1573(76)90032-6.
- [13] P. Francesco Fracassi, G. Cardini, S. O'shea, R. W. Impey, M. L. Klein, Solid and liquid carbon monoxide studied with the use of constant-pressure molecular dynamics, *Phys. Rev. B* 33 (1986) 3441–3447. doi:10.1103/PhysRevB.33.3441.
- [14] N. Fray, B. Schmitt, Sublimation of ices of astrophysical interest: A bibliographic review, *Planetary and Space Science* 57 (2009) 2053–2080. doi:10.1016/j.pss.2009.09.011.
- [15] W. F. Giauque, J. O. Clayton, The heat capacity and entropy of nitrogen: Heat of vaporization. Vapor pressures of solid and liquid., *Journal of the American Chemical Society* 55 (1933) 4875–4889.
- [16] R. D. Goodwin, Carbon Monoxide Thermophysical Properties from 68 to 1000 K at Pressures to 100 MPa, *Journal of Physical and Chemical Reference Data* 14 (1985) 849–932. doi:10.1063/1.555742.
- [17] K. Kelley, U.S. Department of the Interior Bureau of Mines, *Bulletin* 584.
- [18] V. A. Konstantinov, V. G. Manzhelii, V. P. Revyakin, V. V. Sagan, O. I. Pursky, Isochoric thermal conductivity of solid carbon oxide: the role of phonons and 'diffusive' modes, *Journal of Physics Condensed Matter* 18 (2006) 9901–9909. doi:10.1088/0953-8984/18/43/011.
- [19] J. O. Clayton, W. F. Giauque, The heat capacity and entropy of carbon monoxide: Heat of vaporization. Vapor pressures of solid and liquid. Free energy to 5000 K from spectroscopic data, *Journal of the American Chemical Society* 54 (1932) 2610–2626.
- [20] Y. Yamashita, M. Kato, M. Arakawa, Experimental study on the rheological properties of polycrystalline solid nitrogen and methane: Implications for tectonic processes on Triton, *Icarus* 207 (2010) 972–977. doi:10.1016/j.icarus.2009.11.032.
- [21] T. Hughes, Thermal convection and the origin of ice streams, *Journal of Glaciology* 55 (2009) 524–536. doi:10.3189/002214309788816722.
- [22] R. L. Kirk, Diffusion Kinetics of Solid Methane and Nitrogen: Implications for Triton, *Lunar and Planetary Science Conference* 21.
- [23] J. Eluszkiewicz, D. J. Stevenson, Rheology of solid methane and nitrogen - Applications of Triton, *Geophysical Research Letters* 17 (1990) 1753–1756. doi:10.1029/GL017i010p01753.
- [24] J. Eluszkiewicz, On the microphysical state of the surface of Triton, *J. Geophys. Res.* 96 (1991) 19.
- [25] D. Esteve, N. S. Sullivan, N.M.R. study of self-diffusion in solid N₂, *Solid State Communications* 39 (1981) 969–971. doi:10.1016/0038-1098(81)90067-3.
- [26] G. Robuchon, F. Nimmo, Thermal evolution of Pluto and implications for surface tectonics and a subsurface ocean, *Icarus* 216 (2011) 426–439. doi:10.1016/j.icarus.2011.08.015.
- [27] L. A. Young, Volatile transport on inhomogeneous surfaces: I - Analytic expressions, with application to Pluto's day, *Icarus* 221 (2012) 80–88. arXiv:1205.1382, doi:10.1016/j.icarus.2012.06.032.
- [28] L. Trafton, Large seasonal variations in Triton's atmosphere, *Icarus* 58 (1984) 312–324. doi:10.1016/0019-1035(84)90048-4.
- [29] A. R. Dobrovolskis, S. J. Peale, A. W. Harris, Dynamics of the Pluto-Charon Binary, *Pluto and Charon* (1997) 159.
- [30] V. S. Solomatov, Localized subcritical convective cells in temperature-dependent viscosity fluids, *Physics of the Earth and Planetary Interiors* 200 (2012) 63–71. doi:10.1016/j.pepi.2012.04.005.
- [31] W. Landuyt, G. Ierley, Linear stability analysis of the onset of sublithospheric convection, *Geophysical Journal International* 189 (2012) 19–28. doi:10.1111/j.1365-246X.2011.05341.x.
- [32] D. Goluskin, H. Johnston, G. R. Flierl, E. A. Spiegel, Convectively driven shear and decreased heat flux, *Journal of Fluid Mechanics* 759 (2014) 360–385. arXiv:1408.4802, doi:10.1017/jfm.2014.577.
- [33] R. C. A. Hindmarsh, A numerical comparison of approximations to the Stokes equations used in ice sheet and glacier modeling, *Journal of Geophysical Research (Earth Surface)* 109 (2004) F01012. doi:10.1029/2003JF000065.
- [34] D. I. Benn, E. D. J. A., *Glaciers and glaciation*, 2nd edition, Routledge, 2010.
- [35] N. J. Balmforth, R. V. Craster, C. Toniolo, Interfacial instability in non-Newtonian fluid layers, *Physics of Fluids* 15 (2003) 3370–3384. doi:10.1063/1.1611179.
- [36] A. D. Howard, Simulating the development of Martian highland landscapes through the interaction of impact cratering, fluvial erosion, and variable hydrologic forcing, *Geomorphology* 91 (2007) 332–363.
- [37] P. M. Schenk, Thickness constraints on the icy shells of the galilean satellites from a comparison of crater shapes, *Nature* 417 (2002) 419–421.
- [38] O. L. White, P. M. Schenk, A. J. Dombard, Impact basin relaxation on Rhea and Iapetus and relation to past heat flow, *Icarus* 223 (2013) 699–709. doi:10.1016/j.icarus.2013.01.013.
- [39] O. M. Umurhan, A. D. Howard, J. M. Moore, P. M. Schenk, O. L. White, Reconstructing Helene's Surface History - Plastics and Snow, in: *Lunar and Planetary Science Conference - Plastics and Snow*, in: *Lunar and Planetary Science Conference*, 2015, p. 2400.
- [40] R. S. Anderson, M. Dühnforth, W. Colgan, L. Anderson, Farflung moraines: Exploring the feedback of glacial erosion on the evolution of glacier length, *Geomorphology* 179 (2012) 269–285. doi:10.1016/j.geomorph.2012.08.018.
- [41] V. S. Solomatov, Scaling of temperature- and stress-dependent viscosity convection, *Physics of Fluids* 7 (1995) 266–274. doi:10.1063/1.868624.
- [42] M. F. Ashby, R. A. Verrall, *Micromechanisms of Flow and Fracture, and their Relevance to the Rheology of the Upper Mantle*,

- Philosophical Transactions of the Royal Society of London Series A 288 (1978) 59–93. doi:10.1098/rsta.1978.0006.
- [43] D. T. J. Hurle, E. Jakeman, E. R. Pike, On the Solution of the Benard Problem with Boundaries of Finite Conductivity, Proceedings of the Royal Society of London Series A 296 (1967) 469–475. doi:10.1098/rspa.1967.0039.
- [44] E. M. Sparrow, R. J. Goldstein, V. K. Jonsson, Thermal instability in a horizontal fluid layer: effect of boundary conditions and non-linear temperature profile, Journal of Fluid Mechanics 18 (1964) 513–528. doi:10.1017/S0022112064000386.
- [45] S. Chandrasekhar, , Oxford: Clarendon, 1961.
- [46] J. W. Glen, The Creep of Polycrystalline Ice, Proceedings of the Royal Society of London Series A 228 (1955) 519–538. doi:10.1098/rspa.1955.0066.
- [47] O. M. Umurhan, J. M. Moore, W. B. McKinnon, A. D. Howard, F. Nimmo, W. Grundy, S. A. Stern, H. Weaver, C. Olkin, K. Ennico, L. A. Young, Glacial Flow on and onto Sputnik Planum, DPS-47 47 (2015) 210.11.

Appendix A. On the dominance of NH-creep over Coble creep

Volume (NH) and boundary (Coble) diffusional creep mechanisms are (respectively) represented in sum as

$$\dot{\epsilon} = \dot{\epsilon}_v + \dot{\epsilon}_b, \quad (\text{A.1})$$

in which

$$\dot{\epsilon}_v = \frac{42D_{0v}\Omega\sigma}{kTd_g^2} e^{-E_v/kT}, \quad (\text{A.2})$$

$$\dot{\epsilon}_b = \frac{42D_{0b}(2\pi\delta)\Omega\sigma}{kTd_g^3} e^{-E_b/kT}, \quad (\text{A.3})$$

where E_v, E_b are the associated activation energies, D_{0v}, D_{0b} are the measured reference diffusion rates, d_g is grain size, $\Omega = 4.7 \times 10^{-29} \text{m}^3$ is the volume of a single N_2 molecule. The second invariant of the stress-tensor is σ . In Coble creep the quantity $2\pi\delta$ is a measure of the width of the grain boundary through which molecules diffuse and this is assumed to be a few widths of a volume of a single N_2 molecule – thus we take $\delta \approx \Omega^{1/3}$. Laboratory measurements of only volume diffusion parameters (i.e., $D_{0v} = 1.6 \times 10^{-7} \text{m}^2/\text{s}$ and $E_v = 8.6 \text{kJ/mole}$) are available as of the writing of this manuscript. In lieu of these parameters for Coble creep we follow [23, 24] who assume that $D_{0b} = D_{0v}$, while also assuming $E_b = (2/3)E_v$, the latter being a suggestion made originally in [42]. The activation energies may be expressed in terms of activation temperatures respectively as $T_v \equiv E_v/k = 1033 \text{K}$ and $T_a \equiv E_b/k = (2/3)E_v/k = 686 \text{K}$. The point at which the two creep rates are equal defines a relationship between temperature and grain size beyond which NH creep will dominate over Coble creep. Thus, setting $\dot{\epsilon}_v = \dot{\epsilon}_b$ and sorting through the algebra reveals that the critical temperature for this transition (T_{cc}) occurs when

$$T_{cc} = T_b \cdot \frac{1}{\ln(d_g/2\pi\Omega^{1/3})}. \quad (\text{A.4})$$

For a N_2 grain of size 1mm, $T_{cc} = 24 \text{K}$. Thus, given the aforementioned experimental uncertainties, this means under Pluto’s current surface conditions NH creep is likely to

be the dominant operating creep mechanism provided the tangential stresses are well below the power-law regime, a figure currently not well constrained ($< 0.001 - 1 \text{MPa}$).

Appendix B. Infinite Prandtl-number equations

The linearized non-dimensional 2D equations describing the onset of convection in infinite-Prandtl number media is given by

$$0 = -\nabla\Pi + Ra\Theta\hat{z} + \nabla \cdot \nu\nabla\mathbf{u} \quad (\text{B.1})$$

$$\partial_t\Theta - w = \nabla^2\Theta \quad (\text{B.2})$$

$$\partial_x u + \partial_z w = 0. \quad (\text{B.3})$$

Length and horizontal space dimensions x and z are scaled by the layer thickness H , velocity scales are scaled by κ/H , while time-scales are given by κ/H^2 . The quantity Θ represents the deviations from the static conductive temperature profile, i.e., $T(z, z, t) = T_s + \Delta T\Theta - \bar{T}_{0z}z$, in which $\Delta T = H\bar{T}_{0z}$. The Rayleigh number at the base is given as

$$Ra \equiv 1.13 \times 10^{13} \left(\frac{H}{\text{km}}\right)^4 \left(\frac{d_g}{\text{mm}}\right)^{-2} \times \exp\left(-\frac{T_a}{T_b}\right) \left(\frac{\bar{T}_{0z}}{\bar{T}_{0z}^{(ref)}}\right), \quad (\text{B.4})$$

where the reference temperature gradient we adopt is $\bar{T}_{0z}^{(ref)} = 20 \text{K/km}$, the base temperature $T_b \equiv T_s + H\bar{T}_{0z}$ and the activation temperature $T_a = 1030 \text{K}$. We set the surface position $z_s = 0$. The function ν is the viscosity scaled by the viscosity at the bottom of the layer and is an explicit function of the height parameter z and whose exact form here is

$$\nu = \exp\left[\frac{T_a}{T_s - z\bar{T}_{0z}} - \frac{T_a}{T_b}\right]$$

However, to facilitate calculation we adopt for ν the Frank-Kamenskii approximation, e.g. [30], which replaces the Arrhenius form above with a simple exponential, i.e.,

$$\nu = e^{pz}. \quad (\text{B.5})$$

Consequently we identify $\ln p$ as equivalent to the ratio of ν_t/ν_b , the ratio of the top viscosity to the bottom viscosity. This approximation works well when the viscosity differences become greater than a factor of 1. A more detailed calculation utilizing the correct Arrhenius form will be reserved for a future calculation.

We assume a streamfunction formulation for the incompressible perturbation velocity field, i.e., $u = -\partial_z\psi$ and $w = \partial_x\psi$, and we assume steady solutions of the form

$$\Theta(x, z) = \Theta_k(z)e^{ikx} + \text{c.c.} \quad (\text{B.6})$$

and similarly for the streamfunction ψ . The horizontal wavenumber is $k \geq 0$ and the vertical eigenfunctions $\Theta_k(z), \psi_k(z)$ are associated with each wavenumber k .

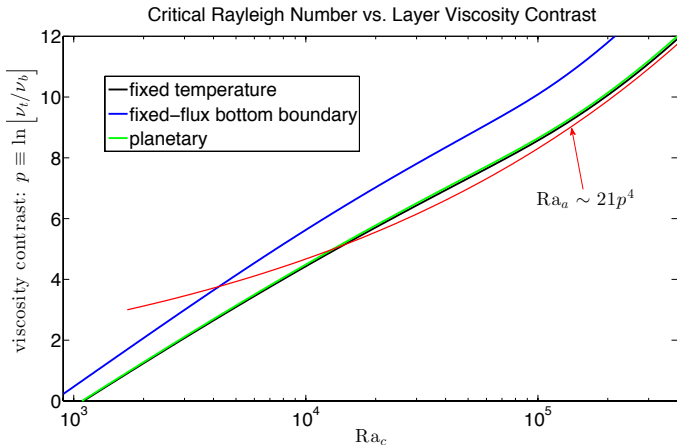


Figure B.15: Critical value of the basal Ra versus viscosity contrast p for the onset of solid-state convection in N_2 ice for parameters shown in Fig. 5. Results for three different boundary conditions are displayed. The asymptotic relationship $Ra_c \approx Ra_a = 21p^4$ is indicated by the red curve.

For kinematic boundary conditions we employ rigid conditions at the bottom boundary $z = 0$, $u = w = 0$ and stress-free, no-normal flow at $z = 1$, $w = \partial_z u = 0$. Owing to the fact that the surface of Pluto today is in vapor pressure equilibrium, we consider it reasonable to impose fixed temperature boundary conditions at the top. This means that $T(z = 1) = T_s$, which translates to $\Theta = 0$ at $z = 1$. The bottom thermal condition, on the other hand, is less clear. If the bottom ice layer interfaces with an active liquid layer (as in solid-state convection models of Enceladus and Europa) then it is reasonable to fix the bottom temperature of the ice layer to the temperature of the top of the liquid layer, which here effectively translates to $\Theta = 0$ at $z = 0$, and henceforth we refer to these as *fixed-temperature* boundary conditions.

However, if the substrate is a static H_2O ice “bedrock”, then the correct boundary conditions become less clear and several options offer themselves here. The substrate presumably passively conducts the geothermal flux emanating from the interior of Pluto and, as such, imposing so-called *fixed-flux* boundary conditions is reasonable, in which $\partial_z T = -\bar{T}_{0z}$ which translates to $\partial_z \Theta = 0$ at $z = 0$. Perhaps, a more physically accurate model is to suppose that the H_2O ice bedrock thermally adjusts to the temperature fluctuations taking place in the convecting ice-layer above. Then following the methodology of [43] we match solutions in the convecting ice-layer onto solutions within the static H_2O ice bedrock. As we noted in Section 2.1 the thermal conductivity of H_2O ice is nearly 20 times that of N_2 ice, i.e., $K_{H_2O} \approx 20K_{N_2}$. Then according to the procedure outlined in [44][43] the bottom boundary condition, in a calculation examining the conditions of onset (i.e., $\partial_t \rightarrow 0$), means imposing

$$\partial_z \Theta_k|_{z=0} = k \Theta_k|_{z=0} (K_{H_2O}/K_{N_2}), \quad (B.7)$$

for every horizontal wavenumber k . We refer to these thermal conditions as *planetary*.

The solution method follows basic procedures, e.g., see [45], except for the fact that the critical values of Ra and corresponding eigenfunctions must be assessed numerically. We solve the resulting one dimensional sixth order system on a Chebyshev grid using standard matrix inversion methods found in all Matlab packages. We have verified the robustness of the solutions by comparing the expected critical Ra number for conditions in which the viscosity is constant. In the instance when both bottom and top thermal boundary conditions are fixed-temperature, together with rigid conditions at the base and stress-free conditions at the top, the transition $Ra = 1101$. Our methods exactly reproduce this value in that case.

We show in Figure B.15 the corresponding critical values of the base Ra (Ra_c) against the value of the viscosity contrast p for the three different thermal boundary conditions described. We also show the asymptotic value of $Ra_c \approx Ra_a = 21p^4$ which is appropriate for temperature dependent Newtonian convection with fixed-temperature boundary conditions at both boundaries [41].

Appendix C. Glacial Model Development

The details of the glacial flow model is presented here.

Appendix C.1. Modeling framework

As we examined in Section 2.2, glacial ice is assumed to have a stress strainrate relationship of the following generic form $\dot{\epsilon} = A\sigma^n$, where $A = A(T)$ and $n = n(T)$, and where σ is the local material stress which is a function of depth from the surface. Using Fig. 7 as a reference, we see that if the gradient of the local surface slopes with a magnitude angle θ with respect to the horizontal, then the corresponding magnitude of the instantaneous stress is given by $\sigma = \rho_s g(z_s - z) \tan \theta$ where, as before, z_s is the height of the local surface located on the map coordinates x, y , i.e. $z_s = Z(x, y, t)$ over time t . The angle θ is given by

$$\sin \theta = S/(1 + S^2)^{1/2}, \quad S \equiv |\nabla Z| = |\tan \theta|. \quad (C.1)$$

In the limit of vanishingly small aspect ratios of (nearly) incompressible flowing materials, it is a fair assumption to approximate the resulting flow as being purely horizontal with no vertical component of velocity. As such, we assume we are in a regime in which SSA is valid. As such, the model procedure in the SSA converts the generic stress-strain relationship into a vertically varying horizontal flow field vector equation, i.e.,

$$\begin{aligned} \frac{\partial \mathbf{u}}{\partial z} &= A \left[\rho_s g (Z - z) \right]^n (\tan \theta)^{n-1} \nabla Z \\ &= A \left[\rho_s g (Z - z) \right]^n S^{n-1} \nabla Z. \end{aligned} \quad (C.2)$$

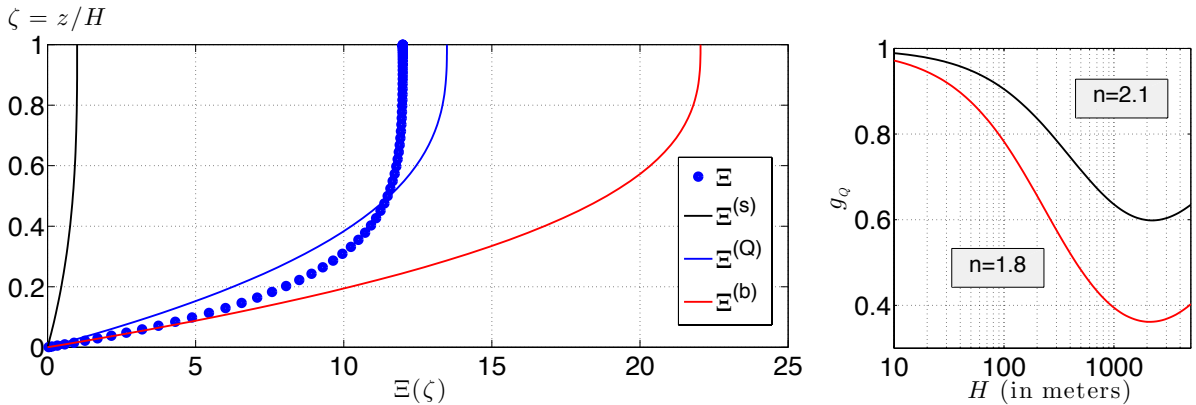


Figure C.16: Left Panel: Comparison of various approximate forms of Ξ . Figure shows the (scaled) vertical shear profile for a rheology with $n = 1.8$, $T_a = 1036\text{K}$, $\bar{T}_{0z} = 20\text{K}/\text{km}$, $T_s = 38.5\text{K}$ and a depth $H = 250\text{m}$. Exact solution (filled circles) compares best with $\Xi^{(Q)}$. Right Panel: The corrective factor g_Q for the two rheologies considered in this paper. Red curve is appropriate for the N_2 ice-grain rheology of [23], where $T_a = 1036\text{K}$, $n = 1.8$, while the black curve is appropriate for the rheology of laboratory annealed N_2 ice of [20], where $T_a = 426\text{K}$, $n = 2.1$.

where the horizontal velocity vector is related to its component velocities via the relationship $\mathbf{u} = u(x, y, t)\hat{\mathbf{x}} + v(x, y, t)\hat{\mathbf{y}}$.

The procedure continues by integrating Eq. (C.2) once to solve for $\mathbf{u}(x, y, t)$, subject to a basal boundary condition. If the ice has not melted (henceforth “dry”), then we assume rigid boundary conditions and assign $\mathbf{u} = 0$ at the base of the layer $z = Z_b(x, y, t) \equiv Z - H$, where $H = H(x, y, t)$ measures the thickness of the ice-layer. Thus

$$\begin{aligned} \mathbf{u}(x, y, z, t) &= \mathbf{u}_{\text{dry}}(x, y, z, t), \\ \mathbf{u}_{\text{dry}} &\equiv \int_{Z_b}^z A \left[\rho_s g (Z - z') \right]^n S^{n-1} \nabla Z dz' \end{aligned}$$

We often will be interested in diagnosing the surface velocities of the flowing ice which we define by $\mathbf{U}(x, y, t) \equiv \mathbf{u}(x, y, Z, t)$.

Given today’s surface temperatures of Pluto ($\sim 38.5\text{K}$), and unless the predominant diameter of N_2 ice grains is much larger than a few millimeters, it is difficult to get basal melt of N_2 before the onset of convection inside a layer. However, as discussed in Earle et al. (2017, this volume) and reviewed in section 2.4, it is possible that the surface temperatures of Pluto’s N_2 ices get high enough so that the base of a N_2 ice layer will exceed its triple point. While the physical properties of N_2 ice glaciers with basal melt represents a wholly new subject matter in which very little is known both experimentally and theoretically, we consider including this possibility in our models using very general considerations borrowed from the literature of terrestrial H_2O ice glaciers. Following [40], we suppose that the base of a N_2 ice layer will slide with a constant (prescribed) velocity, \mathbf{u}_{sl} in a direction prescribed by the gradient of the ice surface *and* only if the depth and basal temperatures exceed the minimum required for N_2 melt.

Thus, we write

$$\mathbf{u}_{\text{sl}} = \begin{cases} u_{\text{sl}0} \hat{\mathbf{t}}, & H > H_m, \\ \mathbf{0}, & 0 < H < H_m, \end{cases} \quad (\text{C.3})$$

in which the map-directional vector $\hat{\mathbf{t}} \equiv \nabla Z / |\nabla Z|$. $u_{\text{sl}0}$ is the speed of the basal flow which is a model input parameter, possibly a function of other inputs. The minimum ice-thickness quantity H_m is a model that takes into account the aforementioned requirements of depth (normal to the ice-layer surface) and surface temperature T_s . For the models examined in this study we will adopt constant values for these quantities, keeping in mind that matters become far more nuanced and complicated when more physical realism is the aim⁹, a goal that will be addressed in future follow-up studies. Nonetheless, in the event that basal melt happens, then the flow velocity field is basally wet, which means it is written as a sum of the dry-field plus the sliding due to basal melt, i.e.,

$$\mathbf{u} = \mathbf{u}_{\text{dry}} + \mathbf{u}_{\text{sl}}. \quad (\text{C.4})$$

The penultimate stage in developing the model involves

⁹ There are many shortcomings of this initial model prescription that ought to be rectified in future modeling. Some of these issues include the following: The first, and probably most important, is the way that mixing of melted N_2 is handled. Liquid N_2 is 20 percent more buoyant than its solid phase, and so the matter of the quality (is it a slush?) and timescale of vertical mixing of liquid N_2 into its solid phase must be addressed in a future detailed physical study. Another matter is the lack of accounting for the bottom topography at the ice-bedrock interface which can, in fact, hinder or alter the ability of the basally melted layer to move at all if, for instance, the bedrock shape is locally upwardly convex which would imply the emergence of a trapped pool/lake of liquid N_2 on the bedrock and lying underneath a covering of solid N_2 . Until the level of the liquid phase reaches the brim of the bedrock bowl, one does not expect net flow due to basal melt. The model as presented here does not distinguish this subtlety.

the formulation of a mass-flux rate \mathbf{q} , defined as a second integral over the ice-layer of mass flux $\rho_s \mathbf{u}$, i.e.,

$$\mathbf{Q}(x, y, t) \equiv \int_{z_b}^Z \rho_s \mathbf{u} dz = Q_0 \nabla Z, \quad (\text{C.5})$$

where the mass-flux scalar prefactor is

$$Q_0 = Q_0(Z_b, H, T_s, T_b, n, \dots),$$

in which T_b is the base temperature of the ice-layer. We explicitly consider the contribution of the mass-flux due to whether or not basal melt is included. This is to say that we identify individual contributions to the mass flux, $\mathbf{Q} = \mathbf{Q}_{\text{sl}} + \mathbf{Q}_{\text{dry}}$, as being a sum derived from basal melt and dry flow. The former of these is

$$\mathbf{Q}_{\text{sl}} = \rho_s H \mathbf{u}_{\text{sl}} = \rho_s H \begin{cases} u_{\text{sl}0} \hat{\mathbf{t}}, & H > H_m, \\ \mathbf{0}, & 0 < H < H_m, \end{cases} \quad (\text{C.6})$$

Below in subsection Appendix C.2 we explicitly examine the form of the dry component of the mass flux \mathbf{Q}_{dry} , as well as the difficulties it admits.

We add the following ingredients: We permit the possibility of a steady form of sublimation/deposition from/onto the surface which we denote by \dot{H}_a . Surface sublimation/deposition is assumed to occur at a uniform rate *in the direction of the local surface normal* - a formulation used in previous landform evolution models e.g., [36, 8]. However we are sensitive to the fact that the true amount of deposition/sublimation is a function of the surface temperatures of the atmosphere, as well as the N_2/CO vapor content of the atmosphere wherein these quantities are, in turn, functions of Pluto's location on its orbit. Despite these caveats, we think it fair to consider this more simpler formulation to investigate the various physical manifestations of basic glacial flow on Pluto's surface. More sophisticated modeling is reserved for future studies.

Additionally, we permit the possibility that a certain amount of the substrate bedrock may be eroded by the moving ice through the processes of scouring or plucking (e.g., [40]) and subsequently absorbed into it and carried along.¹⁰ We represent this erosion/incision rate by \dot{Z}_b and allow for the possibility that it is strictly a function of (i) the total stress exerted at the glacier/bedrock interface if there is no basal melt, (ii) glacial ice sliding speeds if there is basal melt and, possibly, (iii) the total "traffic" of moving ice, defined as $|\mathbf{q}|$. Thus, the complete set equations of motion are

$$\partial_t Z = \nabla \cdot \mathbf{q} + \dot{H}_a + \dot{H}_b, \quad (\text{C.7})$$

$$\partial_t Z_b = -\dot{H}_b, \quad (\text{C.8})$$

¹⁰We realize that this is akin to mixing apples with oranges as H_2O ice has a different density and rheology compared to N_2/CO ice. If the amount of converted substrate bedrock is small compared to the volume of N_2/CO ice, then we consider the results here to be fair and representative of the effective volume present of transportable materials.

in which $\mathbf{q} \equiv \mathbf{Q}/\rho_s$ with $q_0 \equiv Q_0/\rho_s$ together where \mathbf{Q} is given in Eq. (C.5). Because we treat the density as nearly constant, we prefer to follow the rate of change of the local elevation Z instead of the mass-flux rate of change, which is why we have opted to work with the flux quantity \mathbf{q} .

Appendix C.2. Approximate form for dry ice mass-flux and velocities

We examine the form of the velocity fields and corresponding mass-flux in a scenario where there is no basal melt. In the event that both A and n are independent of depth z , then the dry component of q_0 may be evaluated analytically, in which case we say

$$q_0 \rightarrow q_{\text{glen}} \equiv A_c (\rho_s g)^n \frac{H^{n+2}}{n+2} S^{n-1}, \quad (\text{C.9})$$

recovering the familiar Glen law form [46, 34, 47]. Also in this limiting case we can exactly assess both the horizontal velocity field of the dry N_2 ice,

$$\mathbf{u}(x, y, z, t) \rightarrow \mathbf{u}^{(c)}(x, y, z, t) = \frac{A_c H}{n+1} (\rho_s g H)^n \left[1 - \left(\frac{Z-z}{H} \right)^{n+1} \right] S^{n-1} \nabla \mathcal{Z} \quad (\text{C.10})$$

and similarly the surface velocity of the dry flowing ice, i.e.,

$$\mathbf{U}(x, y, t) \rightarrow \mathbf{U}^{(c)}(x, y, t) = \frac{A_c H}{n+1} (\rho_s g H)^n S^{n-1} \nabla Z, \quad (\text{C.11})$$

where the superscript "(c)" denotes the corresponding expression for constant values of $A = A_c$ and n . For the following comparative analysis, it is useful to rewrite the velocity field as as a product of two functions

$$\mathbf{u}^{(c)}(x, y, z, t) = \mathbf{U}^{(c)}(x, y, t) \cdot \Xi^{(c)}(z), \quad (\text{C.12})$$

$$\Xi^{(c)}(z) \equiv 1 - \left(\frac{Z-z}{H} \right)^{n+1}. \quad (\text{C.13})$$

N_2 ice rheologies have temperature dependencies, namely in the pre-factor A and stress-strain exponent n . Given our earlier remarks in Sections 2.3 and 3, and assuming the ice-layers under consideration are not undergoing convection, the interior temperatures increase linearly with depth which makes writing down clean formulae for Q_0 , \mathbf{u} and \mathbf{U} , as in Eqs. (C.9-C.11), unwieldy in most cases - especially when A is characterized as an Arrhenius function of temperature. Nonetheless, to clarify matters and help motivate a useful approximate form, we express the exact solution for \mathbf{u} as a similar product of two functions, i.e.

$$\mathbf{u} \equiv \mathbf{U}^{(c)} \Xi(z), \quad (\text{C.14})$$

where we evaluate $A_c \rightarrow A_s = A(T = T_s) = A(z = Z)$ and letting

$$\Xi(z) \equiv (n+1) \int_{\zeta_b}^{\zeta} \frac{A(\zeta')}{A_s} \left(\frac{Z}{H} - \zeta' \right) d\zeta', \quad (\text{C.15})$$

$$\zeta \equiv z/H, \quad \zeta_b \equiv Z_b/H. \quad (\text{C.16})$$

Our goal then is to develop an approximate solution, $\Xi^{(appx)}$, for the exact vertical structure function $\Xi(z)$ – the latter of which must be determined numerically.

We are reminded that the index n weakly varies with respect to temperature based on the laboratory annealed N_2 experiments of [20], viz. Section 2.2, and that the strongest variations will arise due to the temperature dependence of A . A practical strategy then to handle this is to adopt a constant value of n and consider two end-state values of A : one corresponding to its value based on the surface temperature and one based on the temperature at the base of the layer. In other words, one proceeds by adopting the forms for Q_0 , \mathbf{u} and \mathbf{U} given in Eqs. (C.9-C.11) but replacing A_c with $A_s = A(T_s)$ for the upper end-state and the other lower-end state by replacing A with $A_b = A(T_b)$ where T_b is the bedrock temperature as discussed in Section 3. We consider two choices for the approximate vertical structure function form $\Xi^{(appx)}$: one is where one sets $A(\zeta') \rightarrow A_s$ in the definition found in Eq. (C.15), i.e.

$$\Xi^{(s)} = (n+1) \int_{\zeta_b}^{\zeta} \left(\frac{Z}{H} - \zeta' \right) d\zeta' = \Xi^{(c)}, \quad (C.17)$$

and the second one is $A(\zeta') \rightarrow A_b$

$$\begin{aligned} \Xi^{(b)} &= (n+1)(A_b/A_s) \int_{\zeta_b}^{\zeta} \left(\frac{Z}{H} - \zeta' \right) d\zeta' \\ &= \exp \left[\frac{H/H_a}{1 + H/H_{\Delta T}} \right] \Xi^{(c)}, \end{aligned} \quad (C.18)$$

in which the ratio A_b/A_s was evaluated assuming the generic Arrhenius functional forms posited in Section 2.2. The quantities appearing are $H_{\Delta T} \equiv T_s/\bar{T}_{0z}$ and $H_a \equiv T_s^2/T_a\bar{T}_{0z} = H_{\Delta T} \cdot (T_s/T_a)$. We consider a third possibility, which is similar to $\Xi^{(b)}$ except it is multiplied by a corrective factor $g_{\mathcal{Q}}$ chosen to produce an exact scalar equivalence between the exact mass flux and this approximate form. Thus, we also consider

$$\begin{aligned} \Xi^{(\mathcal{Q})} &= g_{\mathcal{Q}} \Xi^{(b)} \\ g_{\mathcal{Q}} &= \int_{\zeta_b}^{Z/H} \Xi(\zeta) d\zeta \Big/ \int_{\zeta_b}^{Z/H} \Xi^{(b)}(\zeta) d\zeta. \end{aligned} \quad (C.19)$$

As developed, we have three approximate forms of the velocity field \mathbf{u} , i.e. $\mathbf{u} \approx \mathbf{U}^{(c)}\Xi^{(s)}$, $\mathbf{u} \approx \mathbf{U}^{(c)}\Xi^{(b)}$ and $\mathbf{u} \approx \mathbf{U}^{(c)}\Xi^{(\mathcal{Q})}$, and we must now compare these to the exact numerically determined form, $\mathbf{u} = \mathbf{U}^{(c)}\Xi$. Because the horizontal functions $\mathbf{U}^{(c)}$ are the same across all test functions, it will be enough for us to assess the robustness of a given approximation by comparing the three vertical functions $\Xi^{(s)}$, $\Xi^{(b)}$ and $\Xi^{(\mathcal{Q})}$ against the numerically determined exact function Ξ . The left panel of Fig. C.16 shows the vertical structure functions discussed here and as compared to the exact solution determined using a Chebyshev integration method. We see that the exact solution Ξ is well approximated by $\Xi^{(\mathcal{Q})}$. The right panel of the same figure also proves that $\Xi^{(\mathcal{Q})}$ is also well approximated by

$\Xi^{(b)}$, the use of the latter which would incur errors of no more than 50%. The implication of this is that the flow rates and mass-fluxes are reasonably well approximated by a factor of 2 (i.e., $\sim \max(1/g_{\mathcal{Q}})$) when utilizing the rates associated with the higher temperatures corresponding to the base of the layer, i.e., by approximating the velocity field with end-state defined by the base of the layer, $\mathbf{u} \approx \mathbf{U}^{(c)}\Xi^{(b)}$.

Consequently, and from here on out, we adopt the approximate dry ice velocity field constructed from $\Xi^{(\mathcal{Q})}$ and explicitly write out the analytical expressions for the dry components of the N_2 ice mass-flux and velocities to be used in our numerical modeling hereafter: Beginning with the surface dry velocities we have,

$$\begin{aligned} \mathbf{U}(x, y, t) &\approx g_{\mathcal{Q}} \exp \left[\frac{H/H_a}{1 + H/H_{\Delta T}} \right] \mathbf{U}^{(c)}(x, y, t) \\ &= g_{\mathcal{Q}} \exp \left[\frac{H/H_a}{1 + H/H_{\Delta T}} \right] \frac{A_s H}{n+1} (\rho_s g H)^n S^{n-1} \nabla Z, \end{aligned} \quad (C.20)$$

whereupon, the vertically sheared total horizontal flow (dry plus sliding fields) becomes

$$\mathbf{u}(x, y, z, t) \approx \mathbf{u}_{sl} + \mathbf{U}(x, y, t)\Xi^{(c)}(z), \quad (C.21)$$

where $\Xi^{(c)}$ is as given in Eq. (C.13).